Effects of Non-Equilibrium Plasmas on Low-Pressure, Premixed Flames. Part 1: CH* Chemiluminescence, Temperature, and OH

Ting Li, Igor V. Adamovich, Jeffrey A. Sutton[1]

Department of Mechanical and Aerospace Engineering, Ohio State University

Abstract

In this paper, we investigate the effects of nanosecond, repetitively-pulsed, non-equilibrium plasma discharges on laminar, low-pressure, premixed burner-stabilized hydrogen/O_2/N_2 and hydrocarbon/O_2/N_2 flames using CH* chemiluminescence and quantitative OH laser-induced fluorescence (LIF) diagnostics. Two different plasma sources, both of which generate uniform, low-temperature, volumetric, non-equilibrium plasma discharges, are used to study changes in chemiluminescence, temperature, and OH concentration when non-equilibrium plasmas are directly coupled to conventional hydrogen/hydrocarbon oxidation and combustion chemistry. Qualitative imaging of CH* chemiluminescence indicates that during plasma discharge, the luminous flame zone is shifted upstream towards the burner surface with little change in the CH* zone thickness. For the same plasma discharge and flame conditions, quantitative results using spatially-resolved OH LIF and multi-line, OH-LIF thermometry show significant increases in ground-state OH concentrations in the preheating zones of the flame. More specifically, for a particular axial position downstream of the burner surface, the OH concentration increases, which can be viewed as an effective "shift" of the OH profiles towards the burner surface. The increase in OH concentration is conceivably due to an enhancement of the lower-temperature kinetics including O atom, H atom and OH formation kinetics and temperature rise due to the presence of the low-temperature, non-equilibrium plasma.

[1] Corresponding author: sutton.235@osu.edu

Effects of Non-Equilibrium Plasmas on Low-Pressure, Premixed Flames. Part 1: CH* Chemiluminescence, Temperature, and OH

Ting Li, Igor V. Adamovich, Jeffrey A. Sutton
Department of Mechanical and Aerospace Engineering, Ohio State University

1. Introduction

In recent years, considerable interest has focused on studying the enhancement of reactive processes through the coupling of plasma discharges and combustion chemistry [e.g., 1-4] which has come to be known as "plasma-assisted combustion" (or PAC). Many encouraging results have been generated including the demonstration of reduced ignition delay times [e.g., 5-8], increased flame speeds [e.g., 9-13], and increased combustion stability envelopes [e.g., 13-15]; all of which show the potential of plasma discharges in increasing the performance of combustors in a number of energy-conversion systems including power-generating gas turbines and scramjet engines. To put into context the potential benefits of plasma-assisted combustion, Bozhenkov et al. [5] demonstrated a reduction in ignition delay time in H_2/air mixtures by two orders of magnitude (200 μs to 2 μs) using a single high-voltage, nanosecond-duration pulse discharge. While using very low energy input (mJ/cm^3), both Adamovich et al. [6] and Starikovskaya et al. [8] demonstrated a reduction in ignition delay time by more than an order of magnitude, while Starikovskii et al. [7] noted a 600-K reduction in ignition temperature using a similar level of energy input. The same research group also has observed an increase in premixed methane/air flame blow-off velocities by more than a factor of two by the application of a kHz-repetition rate nanosecond plasma discharge. Similarly, flame-speed enhancement has been achieved through nanosecond plasma discharges [9,10] and microwave energy deposition into the flame zone [11]. Dutta et al. [13] demonstrated plasma-assisted ignition and flame holding in cavity flow using nanosecond plasma discharges and showed the improved

performance over a DC arc discharge using same energy input. Laux and co-workers [14, 15] have reported that repetitively-pulsed plasma discharges can significantly reduce the lean flammability limit in turbulent premixed propane-air flames from Φ= 0.7 to 0.3, while Hemawan et al. [16] reported that by coupling low-energy microwave plasmas into the reaction zone of premixed flames, the lean flammability limit was reduced by a factor of five compared to the "un-assisted" combustion cases. It is worth noting that not only have the static stability limits been greatly extended, but conditions normally subject to thermo-acoustic (dynamic) instabilities have been shown to be stable under PAC conditions [e.g., 14, 15]. Simply put, the dynamically-stable operating conditions are extended to leaner conditions in a similar manner as the flammability limits. This implies that the introduction of non-equilibrium plasma discharges directly affects the combustion processes so as to counteract the acoustic/thermal feedback loop which can drive combustion instability dynamics. While these results are quite encouraging, the understanding of the governing physical and chemical processes that lead to the aforementioned results is incomplete, which has led to a limited predictive capability of PAC systems.

The majority of fundamental PAC studies have focused on low-temperature plasma kinetics, including radical and electronically and vibrational-excited metastable species production [17], plasma-fuel oxidation [18-20] and ignition [21-24]. Smirnov et al. [17] showed that by introducing a small number of $O_2(a^1\Delta_g)$ molecules ($\sim$1%) into an H_2–O_2 mixture a noticeable reduction of the ignition delay length and ignition temperature was achieved. Mintusov et al. [18] suggested that the temperature rise in fuel-air mixtures with the presence of plasma discharge is due to exothermic plasma chemical fuel oxidation processes, which results in ignition once the flow temperature reaches the auto-ignition temperature. Yin and co-workers [21-24] investigated low-temperature oxidation and ignition of fuel-air mixtures in the presence

of nanosecond-pulsed plasma discharges using non-intrusive laser diagnostics and detailed numerical simulations. They demonstrated reduced ignition temperatures which were 200 K lower than the auto-ignition temperature under non-plasma-assisted conditions and suggested that the generation of high H-atom concentrations resulted in the observed ignition enhancement.

Fewer studies have directly addressed the effects of highly non-equilibrium plasma discharges on oxidation under higher temperatures, including the effects of plasma discharges on "conventional" combustion chemistry (i.e., moderate and high-temperature reaction kinetics). Notable studies related to this area include the work of Ombrello and co-workers [9, 10] who investigated the plasma-induced chemistry effects of singlet oxygen ($O_2(a^1\Delta_g)$) and ozone (O_3) on flame speed enhancement. Kim et al. [25, 26] investigated hydrocarbon fuel reforming with plasma assistance and suggested that flame stability was enhanced by conversion of CH_4 to H_2 and CO. Rao et al. [27, 28] investigated flames with direct microwave coupling and noted significant increase in OH and CO number densities as microwave powers increased, suggesting high levels of *in situ* fuel reforming of CH_4. Sun et al. [29-31] investigated the effects of nanosecond-pulsed plasma discharges on O-atom production and plasma-assisted methane oxidation under low-temperature conditions within low-pressure, laminar counterflow diffusion flames. Results showed significant increases in O-atom concentration and an extension of the extinction limits in the presence of the plasma discharge.

In a recent collaboration with Georgia Tech, the current authors examined the effects of a pulsed plasma discharge on a single laminar, lean ($\phi = 0.5$) premixed $H_2/O_2/N_2$ flame using high-fidelity numerical simulation and laser diagnostics [32]. The measurements were performed in a novel plasma-flame facility [33] which allows detailed non-intrusive laser-based measurements of temperature and species concentrations to study the interaction between pulsed-plasma

discharges and hydrogen and hydrocarbon flames. In the presence of the plasma discharge, OH mole fractions were found to increase by as much as 500% in the preheat zone and 40% in the post-flame gases of the lean, $H_2/O_2/N_2$ flame. Good agreement was observed between the measurements and numerical results using a one-dimensional, multi-scale, pulsed-discharge model and detailed plasma-combustion kinetics, providing confidence in the numerical model framework. Additional modeling results showed that electron impact dissociation and excitation processes in the plasma have a major impact on the observed species profiles, such that Joule heating alone does not account for the observed effects of the plasma.

To gain an improved understanding of the effects of non-equilibrium plasma discharges on flame chemistry over a broad range of conditions, this manuscript presents quantitative, spatially-resolved measurements of temperature and OH concentration in a series of low-pressure, premixed hydrogen and hydrocarbon flames. For the hydrocarbon flames, additional spatially-resolved CH* measurements are used to complement the temperature and OH measurements to identify plasma-induced changes to global flame structure. First, a detailed assessment of the accuracy of the temperature and OH measurements is presented, followed by temperature/species measurement results over a broad range of operating conditions, including the variation of fuel type, equivalence ratio, and plasma generation characteristics.

2. Plasma-Flame Facility

As described in [33], the over-arching goal of the new plasma/flame facility is to enable the examination of changes in chemical kinetics in the presence of highly non-equilibrium plasmas over a broad range of premixed flame conditions. In addition to variations in global operating parameters including fuel type and equivalence ratio, the low-pressure flame facility allows investigation of the effects of the coupled plasma over a broad temperature range (for any given

fuel or equivalence ratio), corresponding to "distinct" regions within a combustion system including (i) lower-temperature fuel oxidation, (ii) intermediate formation at moderate temperatures in the "preheat" zone, and (iii) high-temperature reaction leading to combustion products.

A water-cooled, 6-cm-diameter McKenna burner [34] is housed within a low-pressure chamber capable of achieving stable (combusting) operating conditions down to 5 Torr. A photograph of the plasma-flame facility is shown in the top panel of Fig 1. The McKenna burner produces a steady, laminar, quasi-one-dimensional flame, which is conducive to both laser-based measurements and numerical modeling with detailed kinetic mechanisms. In this paper, a parametric study covering hydrogen/O_2/N_2 and hydrocarbon/ O_2/N_2 flames operating at different equivalence ratios is performed. The operating characteristics of the investigated flames are given in Table 1. The flow rates of the gases are monitored by calibrated mass flow controllers and the total pressure within the chamber is maintained at a pressure of 25 Torr by a throttled vacuum pump (Welch 1397). In addition, the entire burner facility can be translated in the vertical direction with a resolution of 3 um to facilitate spatially-resolved laser-based measurements as a function of height above the burner surface.

In this facility, we study the direct coupling of steady, laminar, low-pressure premixed flames to highly non-equilibrium, nanosecond-pulsed plasma discharges, which have been studied extensively at Ohio State University [6, 13, 19-24, 35]. By 'direct coupling', we refer to a configuration in which the "entire" combustion process (e.g., fuel oxidation, preheat, high-temperature reaction zone, and products) is encapsulated within the plasma discharge as demonstrated from the visible emission photograph shown in Fig. 1b. As shown in Fig. 1 (bottom), the burner surface acts as the ground electrode and the high-voltage electrode is a 12-

cm-diameter Tungsten mesh (open area = 90%) located 40 mm above the burner surface, which is supported by four ceramic posts mounted to the outer portion of the McKenna burner. In this manner, the high-voltage electrode directly couples the plasma processes to the oxidation and combustion chemistry of interest, while providing minimum disturbance to the laminar flow field and reactant and post-flame gas stream transport. As an example, Fig. 2 shows spatially-resolved OH mole fraction measurements taken within a premixed, $\phi = 1.07$ $CH_4/O_2/N_2$ flame in this facility, with and without the high-voltage electrode in place. The quantitative OH mole fraction measurements are determined using laser-induced fluorescence (LIF) diagnostics; the details of which are given in Sec. 3.2. Also shown in Fig. 2 is the result from a 1D simulation using the PREMIX subroutine [36] within the Chemkin [37] software with the GRI-Mech 3.0 [38] kinetic mechanism. As noted in Fig. 2, there are negligible differences between the OH profiles with and without the upper electrode; thus, it is assumed that the upper (porous) electrode does not disturb the flow or kinetics.

In this manuscript we will describe the use of two high-voltage, nanosecond plasma discharge devices: (1) a short duration (~ 5 ns) fast ionization dynistor (FID) plasma generator and a pulsed-plasma generator developed in-house at OSU, which is based on a high-voltage, high-frequency Behlke MOSFET (metal oxide semiconductor field effect transistor) switch. Figure 3 shows a single-shot voltage pulse shape during FID and "Behlke" pulser operation, measured with a Tektronix P6015A high-voltage probe and Pearson (model 2877) current monitor. As noted in Fig. 3, the pulse width, as defined by the full width at half maximum (FWHM) value, is approximately 7 ns and 170 ns for the FID and Behlke pulsers, respectively. In addition, the estimated pulse energies are ~ 3 mJ/pulse and ~ 1mJ/pulse for the FID and Behlke pulsers, respectively. It is noted that the high-voltage probe has a limited bandwidth (75

MHz), which results in a small (~15%) reduction in the measured peak voltage for the FID pulser, as compared to measurements using a custom higher-bandwdith (1GHz) back current shunt in the coaxial transmission line between the pulser and the load. The reduction in the measured peak voltage for the Belhke pulser is much less due to the longer pulse width. The data shown in Fig. 3 already has been corrected for this effect. In this work, we will consider the effect of 200 sequential FID pulses, each with an inter-pulse separation of 25 μs (pulse repetition rate of 40 kHz) and 800 sequential Behlke pulses, each with an inter-pulse separation of 14.3 μs (pulse repetition rate of 70 kHz).

Figure 4a and 4b show two sets of four instantaneous images of the broadband plasma emission using an intensified CCD camera for the FID and Behlke pulsers, respectively. The images are selected to be representative of the discharge uniformity throughout the plasma burst sequences. The ICCD images were acquired for the "Standard", $\phi = 1.07$, $CH_4/O_2/N_2$ operating condition with the pulsers operating at 40kHz and 70 kHz for FID pulser and Behlke pulser, respectively and the gate time of the ICCD set to 10 ns and 200 ns for FID pulser and Behlke pulser, respectively. Because of the short camera gate, each ICCD image corresponds to a single discharge pulse. As shown in Fig. 4, the large-volume plasma discharge is uniform under the low-pressure and high-temperature conditions considered within the present work. It is noted that the brighter "spot" seen in the upper middle portion of the ICCD images are reflections from the back window and not a region of high plasma emission intensity.

3. Laser-Induced Fluorescence Measurements

3.1 Experimental Setup

Laser-induced fluorescence (LIF) diagnostics are applied to measure quantitative OH mole fraction and temperature distributions within the low-pressure premixed flames with and without the presence of the non-equilibrium plasma discharge. A schematic of the laser and optical setup used for the measurements is shown in Fig. 5. The second harmonic output of an Nd:YAG laser (Spectra-Physics Indi-40-10) at 532 nm is used to pump a tunable dye laser (Sirah Cobra-Stretch) to generate output near 562 nm. The visible output of the dye laser is frequency-doubled using a Type-I BBO crystal to generate tunable ultraviolet output near 281 nm, which is used to excite the (1,0) band of OH $A^2\Sigma^+ - X^2\Pi$ system. The laser linewidth of the UV laser beam was measured as 0.046 cm^{-1} using a high-resolution wavelength meter (High Finesse, Angstrom WS-U). The combination of a half wave plate and a thin-film polarizer is used to attenuate the laser energy to less than 0.4 μJ/pulse to avoid saturation of the excited transitions and remain in the "linear excitation" regime. The UV laser beam then passes through a 500-μm-diameter pin-hole, which defines the spatial resolution of the measurements in the direction normal to the laser beam propagation, and passes into the vacuum chamber through a fused-silica optical access window, oriented near Brewster's angle to minimize the reflections.

For low laser pulse energies, the fluorescence signal is expressed as

$$S_{fl} = n_{OH} \frac{B_{12}}{c} \frac{E}{\Delta \nu_L} f_B \Gamma \phi F_{fl} l \frac{\Omega}{4\pi} \varepsilon \eta \qquad (1)$$

where n_{OH} is OH number density; B_{12} is the Einstein absorption coefficient; c is the speed of light; E is the laser pulse energy; $\Delta\nu_L$ is the laser linewidth; f_B is the Boltzmann factor; Γ is the dimensionless overlap integral between the laser lineshape and the absorption lineshape; Φ is the fluorescence quantum yield; F_{fl} is the fraction of fluorescence bandwidth collected; *l* is the laser path length sampled by the collection optics; ε is the efficiency of the optical system; and η is the efficiency of the detection system.

The fluorescence signal from a region near the center of the flame is collected and focused onto a photo-multiplier tube (PMT; Hamamatsu R9220) by a set of two plano-convex spherical fused silica lenses. Schott glass BG3 and UG11 optical filters are placed in front of the PMT in order to block the broadband flame and plasma emission and allow collection of the OH LIF signal from the A-X (0,0) band near 310 nm only. The individual pulse-to-pulse laser energy fluctuations are monitored with a fast-response photodiode labeled as Photodiode 1 in the schematic in Fig. 5 (Thorlabs DET10A; rise time of 1 ns). Both the OH fluorescence signal and the relative laser energy (the photodiode signal) are collected by a digital oscilloscope (Lecroy Wave Runner 104Xi-A; 1 GHz bandwidth). To infer OH number density from the LIF signal, the fluorescence quantum yield is determined as $\phi = \tau_{fl}/\tau_{rad}$, where τ_{fl} is the measured fluorescence lifetime and τ_{rad} is the collision-free, radiative lifetime. In the present experiments, the fluorescence lifetime is determined by fitting the measured fluorescence signal decay by a single exponential and the radiative lifetime is taken from German [39].

A digital delay generator (Stanford Systems DG 645) serves as the "master clock" for the entire system, sending a 10-Hz, 4-V, 100-μs square-wave trigger signal to the Nd:YAG laser and to the high-voltage nanosecond pulse generator, such that the laser pulse is synchronized to the electric discharge pulse burst. The high-voltage pulse generator (either Belhke pulser or FID pulser) is triggered first to produce a burst of several hundreds of pulses (800 pulses for Belhke pulser, 200 pulses for FID pulser). A second trigger signal is sent to the laser 8 μs after the final electric discharge pulse. This time delay corresponds to the peak LIF signal measured after the discharge pulse, when the plasma emission (primarily N_2 ($C^3\Pi_u \rightarrow B^3\Pi_g$) bands) has decayed to negligible levels.

3.2 OH Mole Fraction Measurements

Relative OH LIF signals from the R1(8) rotational line were used to determine relative OH mole fraction profiles. The signals were recorded by translating the burner within the vacuum chamber while the laser and optics remained at a fixed spatial position and the laser remained at a fixed excitation wavelength. First, the LIF signals were corrected for variations in laser pulse energy, temperature, Boltzmann factor, and the overlap integral as functions of the height above burner. Subsequently, the LIF signal profiles were converted to relative OH mole fraction profiles by normalizing the LIF profiles by a LIF measurement from a well-characterized Φ = 1.07 $CH_4/O_2/N_2$ flame at a height of 12 mm above the burner surface. For each measurement position, fluorescence decay signals for 200 individual laser pulses were recorded and averaged. A short, 6 ns gate was used to minimize the effects of collisional quenching as described in [40-42].

The relative OH mole fraction profiles were placed on an absolute scale by measuring the absolute OH concentration (or mole fraction) at 12 mm above the burner surface by direct laser absorption (OH $A^2\Sigma^+ \leftarrow X^2\Pi$ (v'=0, v''=0) transition) in the Φ = 1.07 $CH_4/O_2/N_2$ flame. The absorption measurement was performed using the Q1 (10) rotational line within OH $A^2\Sigma^+ \leftarrow X^2\Pi$ (v'=0, v''=0) transition near 309.5 nm. The effective laser absorption path length (approximately 65 mm) was determined by 1D OH LIF imaging. Figure 6a shows the fluorescence signal from the flame (Φ = 1.07 $CH_4/O_2/N_2$) with the laser beam placed at 12 mm above the burner surface. As shown in Fig. 6b, the central ~ 45 mm of the OH profile is fairly uniform, but the "wings" of the profile have to be accounted for in the conversion of the OH absorption signal to OH concentration. The procedure used was to determine an "effective" absorption path length, such that the area under the measured 1D OH LIF profile (black curve in Fig. 6b) was the same as that for a uniform OH distribution over an effective path length L (red

line in Fig. 6b). The OH concentration measured using direct absorption under these conditions is 1.4 x 10^{15} molecules/cm^3, which corresponds to a mole fraction of 0.0104 at T=1820 K, which is within 7% of previously published results at the same flame conditions [40]. Referring back to Fig. 2, the measured absolute OH mole fraction profile (following the aforementioned procedure) from the ϕ = 1.07 $CH_4/O_2/N_2$ flame (no plasma discharge) agrees well with the simulation results using the well-known PREMIX subroutine [36] within the Chemkin software [37], suggesting the accuracy of the quantification approach.

3.3 Temperature Measurements

Spatially-resolved temperature profiles were measured for all flames using multi-line OH LIF thermometry. Specifically, the temperature was determined using five rotational lines including the R1(7), R1(8), R1(9), R1(10) and R1(12) transitions of the OH $A^2\Sigma^+ \leftarrow X^2\Pi$ (v'=1, v''=0) system. Instead of recording full LIF excitation spectra for each spatial position above the burner surface, individual OH LIF profiles were determined as a function of the height above the burner surface for fixed laser excitation wavelengths corresponding to the peak of the R1(7), R1(8), R1(9), R1(10) and R1(12) transitions. For each spatial position, the measured intensity was plotted as a function of the rotational energy in a Boltzmann plot to determine the temperature. The burner surface temperature was measured directly using a type-K thermocouple for the flame cases without plasma discharge. For the cases with plasma discharge, the burner surface temperature is assumed to be negligibly affected by the presence of the plasma discharge and the burner surface is assumed to be equivalent to that for the case without plasma.

The discrete temperature measurements at all measured spatial locations were fit to the empirical equation found in previous works [e.g., 40-42]

$$T = A + B\cdot[1 - \exp(C\cdot HAB^{D})] + E\cdot(HAB)^{2} \quad , \qquad (2)$$

where the temperature is in Kelvin, the height above the burner surface (HAB) is in millimeters, and the parameters A to E, shown in Table 2, were determined by least squares fitting. Equation (2) was found to fit the temperature distributions very well, similar to previous work [40-42]. The total uncertainty of the temperature measurements due to the fitting, signal-to-noise, finite spectral resolution of the excitation laser, and the use of fixed-wavelength excitation (vs. full excitation spectra) is addressed in the next section.

4. Measurement Assessment and Uncertainty

Using Eq. (1), the OH mole fraction at any spatial position is determined from the measured OH LIF signal by

$$X_{OH} = X_{OH,ref}\,\frac{S_{fl}}{S_{fl,ref}}\,\frac{E_{ref}}{E}\,\frac{T}{T_{ref}}\,\frac{f_B(T_{ref})}{f_B}\,\frac{\Gamma(T_{ref})}{\Gamma}\,\frac{\tau_{ref}(T_{ref})}{\tau(T)} \qquad (3)$$

where quantities with subscript '*ref*' refer to a reference condition of known mole fraction and temperature; for the current work this is 12 mm above the burner surface of the Φ = 1.07 $CH_4/O_2/N_2$ flame with no plasma. It is noted that the quantification of the OH LIF signal requires the consideration of several temperature-dependent factors, including the Boltzmann factor, electronic quenching due to other species (manifested through the measured fluorescence lifetime τ), and temperature-dependent overlap of the laser line with the Doppler-broadened OH absorption transition (Γ). While the uncertainty of the OH mole fraction measurements is minimized by using the relatively temperature-insensitive R1(8) rotational line, this section addresses the experimental factors affecting the temperature measurements, as the measured temperature is the dominant source of uncertainty in converting measured LIF signals to

quantitative OH mole fractions. In addition, accurate temperature measurements are necessary for assessing purely thermal (heating) and non-thermal (plasma chemistry) effects of the non-equilibrium plasma on the flame environment. Finally, additional uncertainty in the OH mole fraction measurements arising from laser absorption, fluorescence trapping, and absolute calibration are discussed.

4.1 Temperature Uncertainty

To assess experimental factors that can affect the temperature measurements, synthetic OH LIF excitation spectra were calculated using the LIFBASE [43] software for various temperatures, fluorescence detection strategies, instrument resolution, and signal-to-noise ratios. Figure 7 shows spectra calculated at the three representative temperature cases (T=1820 K, 1000 K and 800 K), where two cases are shown in each subplot; that of no noise (SNR=∞) and one with added noise comparable to the measured experimental noise at the specified temperature (SNR=12.1). The experimental SNR of the OH LIF measurements was estimated from a series of measurements at various temperatures, where the SNR was defined as the mean OH LIF signal divided by the standard deviation of the OH LIF signal fluctuations.

As described in Sec 3.3., temperature was determined using multi-line OH LIF thermometry, where measured LIF signals from a fixed laser excitation wavelength corresponding to the *peak* of the targeted rotational lines (labeled in Fig. 7) were used to infer the temperature. Often complete laser excitation scans (LIF intensity vs. wavenumber) are performed such that the total intensity can be integrated over each rotational transition to minimize the effects of instrument resolution and rotational line-specific features. Due to the large number of test cases (see Table 2) and the desire for spatially-resolved measurements as a

function of height above the burner surface, performing detailed laser excitation scans for each spatial position of each test case was not feasible. Figure 8 shows a comparison of temperatures inferred for the synthetic T = 1820 K case using fixed laser wavelength excitation (at the peak of the rotational lines) versus complete laser excitation scans which yield the total integrated contributions of the R1(7), R1(8), R1(9), R1(10) and R1(12) transitions of the A-X (1,0) band of OH. The Boltzmann plot using the total integrated area from each transition is shown with the black symbols and line fit, while the Boltzmann plot using the peak of the laser excitation scans only is shown with the red symbols and line fit. For both of these calculated cases, the spectral resolution is set to 0.001 cm^{-1}, which is well below the Doppler-broadened linewidth of the OH absorption transitions (~ 0.25 cm^{-1}), such that the effects of fixed excitation versus integrated signal detection can be isolated from linewidth effects. For the simulation temperature of T = 1820 K, the temperature inferred from a "simulated" laser scan and integrated signal detection of the five rotational lines results is T_{LIF} = 1822 K, while the inferred temperature resulting from detection of the LIF signal with fixed laser excitation is T_{LIF} = 1827 K. For the current experimental spectral resolution (defined by the laser linewidth) of $\Delta\nu$ = 0.046 cm^{-1} and fixed laser excitation, shown by the blue symbols and line fit, the inferred temperature is T_{LIF} = 1831 K. These calculations show that the use of fixed laser excitation and the current experimental resolution minimally affects the accuracy of the temperature inference from the LIF spectra.

The accuracy of the temperature inferred from the multi-line OH LIF data may be further affected by finite signal-to-noise ratio (SNR). To estimate potential SNR effects, noise comparable to the experimental values was incorporated into the LIFBASE simulation, as indicated in Fig. 7. Boltzmann plots and inferred temperatures for three example simulated temperature conditions are shown in Fig. 9 for the case of no noise (SNR = ∞) and the finite

SNR cases. For each case, fixed laser excitation and the experimental spectral resolution ($\Delta\nu$ = 0.046 cm^{-1}) were simulated. For the two lowest temperature cases (T = 1000 K and 800 K), temperature is inferred from both four and five rotational lines, where for the "four line" case, the R1(12) transition is not used. Figure 9 shows that the experimental noise is more likely to introduce high levels of error using the five rotational lines at low temperatures because R1(12) is very weak at low temperatures and is strongly affected by noise at low temperatures. For the simulated T = 800 K case, the use of the R1(7), R1(8), R1(9), and R1(10) rotational lines only results in an inferred temperature of T_{LIF} = 774 K (3% error) as opposed to an inferred temperature of T_{LIF} = 990 K (23.8% error) when all five rotational lines are used.

Figure 10 shows the total estimated error (ε_T) in temperature by using the multi-line approach inferred from synthetic OH spectra. As shown in Fig. 10, the error is quite small at high temperatures, even for modest SNR values, and increases as temperature is reduced for the current range of SNR levels considered. It is apparent that OH LIF thermometry measurements using the five rotational lines are more accurate at moderate to high temperatures, but results in significant error at temperatures less than 1000 K. However, the temperature inferred using only four rotational lines (without the R1(12) transition) is more accurate in the low-temperature range (see Fig. 10). Therefore, for the current OH LIF thermometry measurements, five-line measurements are used for temperatures greater than 1000 K and four-line measurements are used for temperatures lower than 1000 K.

Because the temperature is determined from the slope of the measured fluorescence intensity as a function of rotational energy, the temperature uncertainty is affected by both uncertainties in the measured intensities and the accuracy of the Boltzmann fit. In addition to measurement noise, the measured intensities are subject to uncertainties due to the overlap of the

laser with the desired absorption transition (at rotational level J) due to laser frequency jitter. These effects are finite but relatively small since 200 laser pulses are averaged for each temperature measurement. Additional experimental artifacts, such as laser attenuation, lead to minor additional uncertainties (~1%) since the laser excites the (1,0) band of OH $A^2\Sigma^+ - X^2\Pi$ system at low number densities. Fluorescence trapping of the emitted fluorescence (near 310 nm) is estimated as 6% of the signal based on laser absorption measurements at similar wavelengths, but its effect on the slope of the Boltzmann plot is much weaker because each rotational line excitation exhibits the same fractional absorption of the fluorescence emission. Fluorescence trapping effects on the inferred temperature are estimated as less than 2% over the entire temperature range. Combining all the aforementioned factors, the uncertainty of the temperature inference is approximately 6% at lower temperatures ($T < 1000$ K) and decreases to approximately 3% in the post-flame gases ($T \sim 1800$ K). While there are no absolute standards to which the results of the present temperature measurements can be compared to assess their accuracy, the $\phi = 1.07$ $CH_4/O_2/N_2$ case is a "GRI-Mech 3.0 [39] target case" that has been studied extensively [e.g., 42-44]. In the present work, a temperature of 1830 K was determined at a height of 12 mm above the burner surface at these conditions. This temperature is compared to temperature values of 1916 K, from Berg et al. [40] and 1890 K from Sutton et al. [41] at a similar spatial position, indicating the precision of the current measurements in comparison to previously-measured results.

4.2 Additional OH Mole Fraction Uncertainties

As noted above, the uncertainty in the OH mole fraction measurements is minimized by using the R1(8) rotational line, which is relatively temperature insensitive. The total uncertainty in the

measured OH mole fraction is estimated by considering the individual uncertainties of the terms in Eq. (3) and treating them as independent error sources.

The uncertainty in $X_{OH,\,ref}$ is 15% based on the direct absorption measurements described in Sec. 3.2. The uncertainty in the ratio $S_{fl}/S_{fl,ref}$ is due to experimental shot noise and wavelength fluctuations, which can slightly displace the probing laser from the peak of the absorption transitions. Both of these factors are determined directly from the measured signal-to-noise ratios, which vary from 8% (at low temperatures and OH mole fractions) to 1.5% (at high temperatures and OH mole fractions). The uncertainty in the Boltzmann factor is determined for the R1(8) rotational line for the previously-determined temperature uncertainties. At a low temperature of 1000 K, a 6% uncertainty in temperature leads to a 6% uncertainty in the Boltzmann factor, while at 1800 K, a 3% uncertainty in temperature leads to < 0.5% uncertainty in the Boltzmann factor. The uncertainty in the overlap integral is due to uncertainties in the temperature (due to the Doppler broadening of the OH absorption line) and laser wavelength fluctuations. Using the previously-determined temperature uncertainty, the uncertainty in Γ is between 1.3% and 1.5% for the temperature range of 800 K to 1900 K. The consideration of wavelength fluctuations equal to that of the laser linewidth ($\Delta\nu$ = 0.046 cm^{-1}) lead to additional uncertainties less than 0.1%. Finally, the uncertainty in the measured fluorescence decay time, τ, is only due to the uncertainty in fitting the measured decay with a single exponential curve. The uncertainty of the fit, as determined from the R^2 value of the fit was less than 1%. The total estimated uncertainty in the OH mole fraction measurements is bound between 20% for low temperatures (OH mole fraction) and 16% for high temperatures (OH mole fraction), where the dominant source of uncertainty is manifested through the absorption measurement to place the OH results on a

quantitative scale. Relative uncertainties are bound between 12% for low temperatures (low OH mole fraction) and 5% for high temperatures (high OH mole fraction).

5. Results and Discussion

5.1 Plasma Effect on CH Chemiluminescence*

For the CH_4- and C_2H_4-based flames, direct flame emission from $CH(A^2\Delta \rightarrow X^2\Pi)$ or "CH* chemiluminescence" is used to assess qualitatively the effect of the non-equilibrium plasma discharges on global flame structure. The CH* emission is collected using an intensified CCD camera (Princeton Instruments PI-MAX 2) in combination with a 10-nm bandpass filter centered at 430 nm. The ICCD images are collected for camera gate of 50 ns, and the average of 200 instantaneous images is reported for each flame. Figure 11 shows three sets of CH* images from the $CH_4/O_2/N_2$ flames corresponding to equivalence ratios of 1.07 (top), 0.81 (middle) and 0.62 (bottom). The images in the left column are acquired without plasma, and the images in the right column are acquired 8 μs after the completion of 200 discharge pulses generated by the FID plasma generator (at 40 kHz pulse repetition rate). The white dashed line represents the location of the burner surface, the red dashed line represents the upstream (i.e. bottom) boundary of the CH* emission without the plasma, and the blue dashed line represents the upstream (bottom) boundary of the CH* emission in the presence of the plasma discharge.

Figure 11 shows that as the equivalence ratio is reduced (i.e. for "lean" conditions), the effect of the electric discharge on the flame emission becomes increasingly noticeable in terms of CH* emission displacement. Figure 12 shows emission intensity distributions along the centerline of the CH* images shown in Fig. 11. For all three equivalence ratios, there is a shift of the luminous CH* zone towards the burner surface in the presence of the plasma discharge,

where the shift between the cases with and without the plasma increases with decreasing equivalence ratio. For the $\phi = 0.62$ flames, a comparison of the CH* emission profiles for the cases with and without the plasma indicates that the luminous CH* zone shifts towards the burner surface by approximately 2 mm when the FID electric discharge is applied. While the CH* zone shifts toward the burner surface with the application of the non-equilibrium plasma discharge, there is no appreciable increase in the width of the CH* zone.

Figure 13 shows three sets of CH* chemiluminescence images from three $C_2H_4/O_2/N_2$ flames corresponding to equivalence ratios of 1.07 (top), 0.81 (middle), and 0.52 (bottom). The images in the left column are acquired without plasma, and the images in the right column are acquired 8 μs after the completion of 200 pulses generated by the FID plasma generator (at 40 kHz pulse repetition rate). Figure 14 shows the corresponding emission intensity distributions along the centerline of the CH* images shown in Fig. 13. Similar to the results in CH_4 flames (see Figs. 11 and 12), there is a noticeable 1.5-mm shift of CH* emission toward the burner surface with the plasma on at the leanest ($\phi = 0.52$) condition, although the effect at the $\phi = 0.81$ and $\phi = 1.07$ conditions is smaller compared to the CH_4-based flames. For the $\phi = 0.81$ and $\phi = 0.52$ cases, there is a small, but discernable narrowing of the CH* zone thickness in the presence of the plasma discharge, as determined from the intensity distributions in Fig. 14. Assuming that the CH* emission is a suitable marker for the peak heat-release zone in lean, premixed flames, the results suggest a direct effect of the electric discharge on flame chemistry.

For both the $CH_4/O_2/N_2$ and $C_2H_4/O_2/N_2$ flames, it is noted that there is no appreciable increase in the magnitude of the CH* emission intensity for the cases with plasma compared to the cases without plasma. While CH* emission images are not quantitative, the images for the cases with and without the plasma discharge are collected with the same camera settings, such

that relative differences between the two emission profiles can be compared. The observation that the CH* emission magnitudes are the same for the cases with and without plasma is in contrast to previous results under similar flame conditions in the same facility [34] when CH* emission was measured *during* the plasma discharge. In Ref. [34], an increase in the peak CH* signal of 67% was measured in a $\phi = 0.8$ $CH_4/O_2/N_2$ flame operating at 20 Torr using the FID plasma discharge at 10 kHz. As noted above, the present CH* images (as well as OH LIF measurements discussed below) are acquired 8 μs after the end of the discharge pulse burst , which corresponds to both a maximum of OH LIF signal and the complete decay of the plasma emission (primarily N_2 ($C^3\Pi_u \rightarrow B^3\Pi_g$) bands). The observation of no increase in the CH* emission magnitude after the discharge pulse burst and nearly complete decay of the plasma emission is consistent with the fact that the increase in the excited-state species population such as CH* occurs only during the operation of the pulsed discharge. Furthermore, since the peak increase in the measured OH LIF signal occurs 8 μs after the end of the discharge pulse burst (while the excited-state species populations such as CH* return back to their baseline values), it is inferred that plasma effect on the ground-state species populations (such as measured via LIF) occurs on a longer timescale compared to its effect on the excited-state species populations (detected inferred from chemiluminescence data).

5.2 Plasma Effect on OH and Temperature Profiles in Hydrocarbon Flames

Figure 15 shows the measured temperature and OH mole fraction profiles for the three $CH_4/O_2/N_2$ flames, at equivalence ratios of 1.07, 0.81, and 0.62, without the plasma (black symbols), with plasma generated by the Belhke pulser (blue symbols), and with plasma generated by the FID pulser (red symbols). The results obtained in the presence of the plasma

discharges are measured 8 μs after 800 consecutive pulses (70 kHz) and 200 consecutive pulses (40 kHz) from the Belhke and FID pulsers, respectively. For the temperature results (left column), the average from 200 individual measurements are shown with the solid symbols, while the solid lines represent the least square fits to the data using the formulation of Eq. (2) and the parameters listed in Table 2. For the OH results (right column), the measured fluorescence signal is converted to mole fraction using the methodology described in Sec. 3.2. The solid symbols represent the average from 200 individual measurements and the dashed line is the result from a 1D simulation of the flame with no plasma using the PREMIX subroutine [36] within the Chemkin [37] software with the GRI-mech 3.0 [38] kinetic mechanism. For the PREMIX calculation, the simulated results are obtained by using the measured temperature profile as an input to isolate kinetic effects.

The results in the $CH_4/O_2/N_2$ flames using both FID and Behlke plasma generators demonstrate an increase in the temperature and OH mole fraction over a range of heights above the burner surface compared to the conditions without the plasma. Figure 15 shows that the effect of the plasma increases as the equivalence ratio is reduced. As one example, for the ϕ = 0.62 flame condition, both the temperature and the OH profiles shift towards the burner surface by approximately 2 mm, compared to the case without the plasma, consistent with the CH* imaging results shown in Fig. 11. In addition to a strong dependence on equivalence ratio, the effect of the plasma is highly dependent on the spatial position. The left column in Fig. 16 shows the difference between the measured gas temperature profiles ($\Delta T = T_P - T_{NP}$) for the cases with the plasma discharge (T_P) and without the plasma discharge (T_{NP}) as a function of height above the burner surface (HAB) for both plasma generators. The right column of Fig. 16 shows the normalized difference in OH mole fraction for both plasma generators, defined as

$\Delta X_{OH,norm} = (X_{OH,P} - X_{OH,\ NP})/X_{OH,NP}$, where $X_{OH,P}$ is the measured OH mole fraction profile without plasma and $X_{OH,NP}$ is the measured OH mole fraction profile with plasma. In general the results of Fig. 15 and 16 show that the effect of the plasma is maximum in the preheating region (i.e., at HAB < 8 mm), both for temperature and for OH mole fraction. In the ultra-lean flame case (ϕ = 0.62), where the plasma has the strongest effect, the temperature in the preheating region (HAB < 8 mm) increases by approximately 370 K and the OH mole fraction increases by as much as 300%. In the post-flame region (e.g., at HAB > 10 mm), temperature increases by only 50 K-150 K and OH mole fraction increases by ~10%-20%.

In the presence of the plasma discharge, significant amounts of O and H are generated via direct electron impact and the quenching of excited electronic states of nitrogen, N_2*; for example:

$$e + CH_4 \Rightarrow CH_3 + H + e \quad \text{(R1)}$$

$$e + O_2 \Rightarrow O + O + e \quad \text{(R2)}$$

$$e + O_2 \Rightarrow O + O(D) + e \quad \text{(R3)}$$

$$e + N_2 \Rightarrow N_2^* + e \quad \text{(R4)}$$

$$N_2^* + CH_4 \Rightarrow N_2 + CH_3 + H \quad \text{(R5)}$$

$$N_2^* + O_2 \Rightarrow N_2 + O + O \quad \text{(R6)}$$

These processes form chemically-reactive radicals (e.g., O and H) and lead to chain initiation and branching reaction (e.g., $CH_4 + O = CH_3 + OH$; $H + O_2 = OH + O$) at lower temperatures, which do not readily occur under conventional flame conditions. In addition, heat generated by plasma-induced exothermic fuel oxidation reactions increases the gas temperature and accelerates "conventional" oxidation and combustion reactions, which are highly sensitive to temperature. Due to these effects, species such as OH form closer to the burner surface, resulting

in an effective "shift" of the temperature and OH mole fraction profiles, which is consistent with the experimental results shown in Figs. 15 and 16.

While the FID and Belhke pulsers produce similar temperature and OH mole fraction increases for the leanest, ϕ = 0.62 $CH_4/O_2/N_2$ flame, there are differences between the results using the Belhke and FID plasma generators for the ϕ = 0.81 and 1.07 cases. For a given equivalence ratio, the effect on the temperature profile caused by different plasma generators is different, unlike the OH mole fraction profile. For the ϕ = 1.07 case, the use of the FID pulser produces a temperature rise of approximately 150K at HAB = 4 mm, which increases monotonically to about ΔT = 160 K at further downstream positions measured, up to HAB = 20 mm. In comparison, the Belhke pulser produces a peak temperature rise of ~ 60 K at HAB = 2 mm, which then decreases to ΔT = 20 K at HAB = 6 mm, and then increases again to ~ 60K at HAB = 20 mm. For the same ϕ = 1.07 flame condition, the FID and Belhke pulsers increase the peak OH mole fraction by ~ 60% and ~ 10%, respectively, at HAB = 3 mm. An interesting case is the ϕ = 0.81 $CH_4/O_2/N_2$ flame, as both the FID and Belhke pulsers produce nearly identical temperature rise in the pre-heating region and very similar temperature rise over the entire spatial domain. However, the increase in peak OH mole fraction is ~ 100% when using the FID pulser compared to an increase in peak OH mole fraction of only ~ 30% when using the Belhke pulser.

The operational characteristics of the FID and Belhke pulsers (200 vs. 800 pulses, respectively) were chosen such that approximately the same total energy (0.6 and 0.8 Joules, respectively) was coupled during a single discharge burst into the entire volume encapsulated between the burner surface and the high-voltage electrode placed 40 mm downstream of the burner surface. In Ref. [32], numerical simulations of a ϕ = 0.5 $H_2/O_2/N_2$ flame showed that only a small fraction of the total time-averaged power was coupled into the preheat region. While it is

difficult to estimate the fraction of discharge power coupled into the preheat region for the current $CH_4/O_2/N_2$ flames (without detailed numerical simulation similar to that presented in [32]), if it is assumed that the same fraction of energy is coupled into the preheat zone for both the FID and Belhke pulsers, then the discharge power coupled into the preheat region is approximately 1.6 times higher for the FID pulser compared to the Belhke pulser. In addition, since the peak pulse voltage generated by the FID pulser is much higher compared to that of the Behlke pulser (almost by a factor of 4, see Fig. 3), the reduced electric field in the preheat zone, E/N, where N is the local number density, also is much higher. Since the rates of electron impact processes scale exponentially with E/N, this results in significantly higher yields of H and O atoms, as well as excited-electronic states of nitrogen, N_2*, in reactions R1-R4, and consequently in reactions R5-R6. This, in turn, results in higher number density of OH formed in subsequent reactions, such as H atom abstraction from CH_4. Comparison of OH measurement results for the FID and Belhke pulsers in Figs. 15 and 16 is consistent with this interpretation; O-atom measurements in the same flames using the two different pulsers will be presented in a forthcoming companion paper [44].

Another critically-important point apparent from the results shown in Fig. 16 is that the effect of the plasma on temperature and OH mole fraction distributions is non-thermal. The temperature rise in the preheat zone of lean and ultra-lean flames increases considerably as the equivalence ratio is reduced, up to $\Delta T \approx 250$-270 K at $\phi = 0.81$ and $\Delta T \approx 350$-370 K at $\phi = 0.62$, much higher compared to temperature rise in the "standard" flame, $\phi = 1.07$ ($\Delta T \approx 60$-140 K). Since the discharge power remains nearly the same over this range of equivalence ratios, this demonstrates that the observed temperature rise is not caused by a trivial effect of input energy thermalization in the discharge (i.e. Joule heating). Since the trend for enhanced temperature rise

in lean and ultra-lean flames correlates with much higher relative increase in OH mole fraction (see Fig. 16), this strongly suggests that the effect is caused by chemical reactions among radical species generated in the plasma. Quantitative analysis of this effect requires detailed kinetic modeling analysis, such as has been done for H_2-O_2-N_2 flames in Ref. [32].

Figure 17 shows the temperature and OH mole fraction profiles measured in three $C_2H_4/O_2/N_2$ flames, at equivalence ratios of 1.07, 0.81, and 0.52, without the plasma (black symbols), with plasma generated by the Belhke pulser (blue symbols), and with plasma generated by the FID pulser (red symbols). Similar to the $CH_4/O_2/N_2$ results shown in Figs. 15 and 16, the $C_2H_4/O_2/N_2$ flame results obtained in the presence of the plasma discharges are measured 8 μs after 800 consecutive pulses (70 kHz pulse repetition rate) and 200 consecutive pulses (40 kHz pulse repetition rate) from the Belhke and FID pulsers, respectively. The average temperature results (solid symbols; left column) are from 200 individual measurements and the solid lines represent the least square fits to the measurements using the formulation of Eq. (2) and the parameters listed in Table 2. For the OH results (right column), the solid symbols represent the average from 200 individual measurements and the dashed line is the result from a 1D simulation of the flame with no plasma using the PREMIX subroutine [36] within the Chemkin [37] software with the GRI-mech 3.0 [39] kinetic mechanism. Similar to the results shown in Fig. 15, the simulated results using PREMIX are obtained by using the measured temperature profile as an input.

Consistent with the results in the $CH_4/O_2/N_2$ flames, both the FID and Behlke plasma generators lead to an effective shift of the temperature and OH profiles towards the burner surface, where the plasma effect increases as the equivalence ratio is reduced and the strongest effect is observed in the lower-temperature (preheat) region. The shift in the OH and

temperature profiles within the $C_2H_4/O_2/N_2$ flames is consistent with the CH* emission imaging results shown in Figs. 13 and 14, where a 1.5-mm shift of the bottom boundary of the emission region toward the burner surface is detected for the $\phi = 0.52$ flame enhanced using the FID plasma generator. While the general trends are similar between the $CH_4/O_2/N_2$ and $C_2H_4/O_2/N_2$ flames, the plasma effect is less pronounced in the $C_2H_4/O_2/N_2$ flames. This is apparent from Fig. 18, which shows the difference between the measured gas temperature and OH profiles for the cases with and without plasma discharge as a function of HAB. For the ultra-lean $C_2H_4/O_2/N_2$ case ($\phi = 0.52$), where the plasma has the strongest effect, the temperature in the preheating region (HAB < 8 mm) increases by 180 K and the OH mole fraction increases by 180%. This is compared with peak ΔT and $\Delta X_{OH,norm}$ of 370 K and 300%, respectively, in the $\phi = 0.62$ $CH_4/O_2/N_2$ flame when using the FID plasma generator.

An additional difference between the $CH_4/O_2/N_2$ and $C_2H_4/O_2/N_2$ flames is the relative effect of the FID and Belhke pulsers. For the $CH_4/O_2/N_2$ flames, the differences in the ΔT and $\Delta X_{OH,norm}$ profiles produced using these two pulsers were notable at $\phi = 1.07$ and 0.81, but decreased as the equivalence ratio decreased. As an example, at equivalence ratios of 1.07, 0.81, and 0.62, the peak $\Delta X_{OH,norm}$ was 70%, 100%, and 300%, respectively, when using the FID pulser and 15%, 30%, and 300%, respectively, when using the Belhke pulser. This corresponds to a ratio of peak $\Delta X_{OH,norm}$ of the FID and Belhke pulsers of approximately 4.6, 3.3, and 1 for $\phi = 1.07$, 0.81, and 0.62, respectively. For the $C_2H_4/O_2/N_2$ cases, at equivalence ratios of 1.07, 0.81, and 0.52, the peak $\Delta X_{OH,norm}$ was 15%, 40%, and 180%, respectively, when using the FID pulser and 15%, 25%, and 60%, respectively, when using the Belhke pulser. This corresponds to a ratio of peak $\Delta X_{OH,norm}$ of the FID and Belhke pulsers of approximately 1, 1.6, and 3 for $\phi = 1.07$, 0.81, and 0.52, respectively. Whereas there were no discernable differences between the

ΔT and $\Delta X_{OH,norm}$ profiles when using the FID and Belhke pulsers at the lowest equivalence ratio ($\phi = 0.62$) in $CH_4/O_2/N_2$ flames, the FID pulser produces a much more pronounced effect in the $\phi = 0.52$ $C_2H_4/O_2/N_2$ flame, compared to the Belhke pulser. Again, quantitative insight into the significant difference between OH number density produced by two different pulse waveforms requires detailed kinetic modeling analysis.

5.3 Plasma Effect on OH and Temperature Profiles in Hydrogen Flames

In Ref. [32], OH and temperature measurement results were presented in a single $\phi = 0.5$ $H_2/O_2/N_2$ flame enhanced using the FID plasma generator. In this section, additional $H_2/O_2/N_2$ flame results are presented using the Belhke pulser at $\phi = 0.5$ and for both the FID and Belhke plasma generators at $\phi = 0.81$. Figure 19 shows the temperature and OH mole fraction profiles measured in two $H_2/O_2/N_2$ flames at equivalence ratios of 0.81, and 0.50. The black symbols are the results without plasma discharge, the blue symbols are the results using the Belhke plasma generator, and the red symbols are the cases using the FID plasma generator. For the temperature results (left column), the solid lines represent the least square fits to the data using the formulation of Eq. (2) and the parameters listed in Table 2. For the OH results (right column), the measured fluorescence signal is converted to mole fraction using the methodology described in Sec. 3.2. The trends shown in the premixed hydrogen flames are the same as the hydrocarbons flames; that is, as the equivalence ratio is reduced, the effect of the plasma discharge increases. However, for $H_2/O_2/N_2$ flames, the effect of the plasma discharge on OH enhancement is greater compared to the hydrocarbon flames. For example, Fig. 20 shows the difference between the measured gas temperature and OH profiles for the cases with and without plasma discharge as a function of HAB, which are denoted as ΔT and $\Delta X_{OH,norm}$, respectively

(similar to Figs. 16 and 18 for the hydrocarbon flames). For the equivalence ratio of $\phi = 0.50$, the FID plasma generator leads to a peak $\Delta X_{OH,norm}$ of 500%, which is compared to a peak value of $\Delta X_{OH,norm}$ of 300% in the leanest $CH_4/O_2/N_2$ flame at $\phi = 0.62$. In addition, the post-flame $\Delta X_{OH,norm}$ in the hydrogen flames is > 30%, whereas the highest post-flame $\Delta X_{OH,norm}$ in the hydrocarbon flames was ~ 15% (see Figs. 16 and18). It is noted that the peak value of $\Delta X_{OH,norm}$ produced by the FID pulser at $\phi = 0.5$ is almost an order of magnitude higher compared to that measured at $\phi = 0.81$ (~500% vs. 50% at HAB of 5 mm), in spite of the temperature increase at this location being almost the same for both cases (see Fig. 20). This is an additional illustration that the observed effect is caused by plasma chemical reaction rather than by purely thermal effect of energy dissipation in the discharge.

For the hydrogen flames, the Belhke and FID plasma generators produce very similar temperature and OH increases at $\phi = 0.81$, but at $\phi = 0.5$, the FID plasma generator leads to a peak $\Delta X_{OH,norm}$ that is over six times higher than that produced by the Belhke plasma generator. This is an interesting result considering that the temperature rise produced by both plasma generators at the spatial location (~5 mm HAB), corresponding to the peak $\Delta X_{OH,norm}$, is very similar, and that the temperature rise profile for $0 < HAB < 5$ mm was much higher when using the Belhke plasma generator compared to the FID plasma generator.

In Ref. [32], a detailed reaction path-flux analysis for the $\phi = 0.5$ $H_2/O_2/N_2$ flame was presented. The results showed that the electric discharge generates considerable amounts of O atoms via direct electron impact ($e + O_2$) and by quenching of excited-electronic states of N_2 by O_2 ($N_2^* + O_2$), as well as H atoms via electron impact ($e + H_2$). The significant increase of O (and H) atom number densities accelerates chain initiation and branching at lower temperatures, via reactions $H + O_2 \Rightarrow OH + O$ and $O + H_2 \Rightarrow OH + H$, which lead to the increased OH

concentrations. In addition, OH is formed by the increased occurrence of reactions between O and H with HO_2. The results in Figs. 19 and 20, as well as the path flux analysis presented in Ref. [32], suggests that the FID plasma generator is much more efficient for production of O atoms compared to the Belhke plasma generator at very lean conditions, which leads to more efficient generation of OH radicals in subsequent chemical reactions. This effect is almost certainly caused by much higher pulse peak voltage and reduced electric field produced by the FID pulser (see Fig. 3). In a forthcoming publication [45], direct measurements of O atom produced using both the Belhke and FID plasma generators in the hydrocarbon and hydrogen flames will be presented.

5.4 Brief Comments on Joule Heating vs. Plasma Kinetics

A fundamental issue of plasma-assisted combustion studies is the underlying mechanism in which non-equilibrium plasma discharges "enhance" combustion processes: thermal or kinetic. In Ref. [32], a first attempt at examining this issue in the current set of flames was performed using numerical simulation of the ϕ = 0.5 $H_2/O_2/N_2$ flame in the presence of the electrical discharge for a case with electron impact excitation and dissociation processes included in the kinetic model and for a case without electron impact processes. For the case where the electron impact processes are not included, the only plasma effect is purely thermal "Joule heating"; that is, discharge input power is directly converted to heat. Considerable difference between the predicted temperature, OH, H, and O profiles in the ϕ = 0.5 $H_2/O_2/N_2$ flame was predicted by the model with and without the consideration of the electron impact kinetics, especially in the preheat region (HAB < 15 mm) [32], suggesting that plasma chemical reactions and the

corresponding heat release are at least partly responsible for the observed effects, rather than Joule heating alone.

In the present work, temperature and OH measurements show that the effect of the plasma becomes more pronounced as the equivalence ratio is reduced for all flame conditions considered. However, nearly the same amount of energy is coupled to the flame by the discharge for all equivalence ratios studied. In this manner, it is expected that the contributions from Joule heating would be nearly constant for all equivalence ratios, including the $\phi = 1.07$ hydrocarbon flame cases where essentially no plasma effect was observed. The present experimental results, which show a significant equivalence ratio dependence on plasma enhancement (determined from temperature and OH increases), is consistent with the previous conclusion from Ref. [32] that plasma chemical processes play a key role in radical production/enhancement, especially in the preheat region, and that the observed effect is not due to Joule heating alone. The forthcoming results on O-atom production in a companion paper [44] will be used to further illustrate this conclusion.

5. Summary and Conclusions

This paper presented an extensive set of CH*, temperature, and OH mole fraction measurements in a plasma/flame facility focusing on the effects of repetitively-pulsed, nanosecond-duration, electric discharges on low-pressure, laminar, premixed, burner-stabilized flames. Two plasma generators were used which differed in pulse duration, peak voltage, and coupled energy per pulse. However, both nanosecond-pulse plasma generators were shown to produce uniform and volume-filling plasma discharges and the repetition rate and number of discharge pulses was

varied between the two different configurations such that nearly the same total energy is coupled to the flame during a single discharge burst.

For lean CH_4 and C_2H_4 flames, the measured CH* emission intensity shifts spatially toward the burner surface when the plasma discharge is activated. Assuming that the excited-state CH* emission is a suitable marker for the region of peak heat release; the results indicate a direct effect of the electric discharge on flame chemistry. OH laser-induced fluorescence measurements were used to determine temperature and absolute OH mole fraction spatial distributions as a function of the height above the burner surface with and without the plasma discharge for methane, ethylene, and hydrogen flames at different equivalence ratios. For both the hydrogen and hydrocarbon flames, the effect of the plasma discharge increases significantly as the equivalence ratio decreases. More specifically, increases in OH mole fractions as high as 150%, 300%, and 500% are determined in the preheat regions near the burner surface for the leanest ethylene, methane, and hydrogen flames, respectively. In addition, the peak temperature and OH mole fraction, which are attained in the post-flame gases for burner-stabilized flames, increase as well in the presence of the plasma discharge. The increase in OH mole fraction for a particular spatial position downstream of the burner surface can be viewed as an effective shift of the OH profiles towards the burner surface. For the lean hydrocarbon flames, the spatial shifts in OH profiles are consistent with the shift measured from the CH* emission imaging.

While the qualitative trends of the plasma enhancement was similar between the two plasma generators, the quantitative effects in terms of absolute temperature and OH mole fraction increases varied between the two plasma generators. For all cases, the shorter-pulse duration (~7 ns), higher peak voltage (~14 kV), higher-coupled energy (~3 mJ/pulse) FID plasma generator led to higher increases in OH mole fraction compared to the Belhke plasma generator

(~170 ns pulse duration; ~ 3 kV peak voltage, ~ 1 mJ/pulse coupled energy), although the operational characteristics of the Belhke plasma generator (800 vs. 200 sequential pulses) were set such that approximately the same total energy was coupled to the flame. Based on the present experimental results and previous kinetic modeling [32], the electric discharge generates significant amounts of O and H atoms via direct electron impact, as well as quenching of excited-state species, which accelerates chain initiation and chain branching reactions at low temperatures (i.e. in the preheat region below the flame in the present burner-stabilized flames). When comparing the FID and Belhke plasma generators, higher reduced electric field (E/N) produced by the FID plasma generator leads to more efficient ionization and production of excited species and atoms (O and H) by electron impact reactions, which subsequently produce larger amounts of OH.

Finally, it is noted that the present measurements support the conclusion that the observed effects are due at least partly to plasma chemical processes (i.e., enhanced radical production at low temperatures), rather than Joule heating alone. For a given set of reactants, the amount of energy coupled to the flame is essentially the same for all equivalence ratios tested, and thus the Joule heating effect should be comparable across the entire range of the equivalence ratios. However, the present measurements demonstrate a significant equivalence ratio dependence of the relative increase in gas temperature and OH mole fraction (or number density) in the presence of the non-equilibrium discharges. Future measurements of O-atom concentrations in the same set of flames will be used to further illustrate this conclusion.

Acknowledgements

The support of AFOSR MURI grant FA9550-09-1-0602 (Chiping Li – program monitor) is greatly appreciated.

References

1. Stockman, E.S., Zaidi, S.H., Miles, R.B., Carter, C.D., Ryan, M.D., Measurement of Combustion Properties in a Microwave Enhanced Flame, Combustion and Flame 2009 156(7) 1453-1461Kosarev, I.N., Aleksandrov, N.L., Kindysheva, S.V., Starikovskaia, S.M., Starikovskii, Yu. A. Kinetics of Ignition of Saturated Hydrocarbons by Nonequilibrium Plasma: CH_4-containing Mixtures, Combustion and Flame 2008 154, 569
2. Starikovskaia, S.M., Kukaev, E.N., Kuksin, Nudnova, M.M., Starikovskii, Yu. A. Analysis of the Spatial Uniformity of the Combustion of a Gaseous Mixture Initiated by a Nanosecond Discharge, Combustion and Flame 2004, 139, 177
3. Starikovskii, A., Anikin, N., Kosarev, I., Mintoussov, E., Nudnova, M., Rakitin, A., Roupassov, D., Starikovskaia, S., Zhukov, V., Nanosecond-Pulsed Discharges for Plasma-Assisted Combustion and Aerodynamics, Journal of Propulsion and Power, 2008, 24, 118
4. Sun W., Ju Y., Nonequilibrium Plasma-Assisted Combustion: A Review of Recent Progress. J. Plasma Fusion Res. Vol.89, No.4 (2013) 208-219
5. Bozhenkov, S.A., Starikovskaya, S.M., and Starikovskii, Yu. A., Nanosecond Gas Discharge Ignition of H_2 and CH_4 Containing Mixtures, Combustion and Flame 2003, 133, 133.
6. Adamovich, I.V., Choi, I., Jiang, N., Kim, J.H., Keshav, S., Lempert, W.R., Mintusov, E., Nishihara, M., Samimy, M., Uddi, M., Plasma Assisted Ignition and High-Speed Flow Control: Non-Thermal and Thermal Effects, Plasma Sources Science and Technology 2009, 18, 034018.
7. Starikovskii, A.Yu., Plasma Supported Combustion, Proceedings of the Combustion Institute 2005 30, 2405
8. Starikovskaya, S.M., Aleksandrov, N.L., Kosarev, I.N., Kindysheva, S.V., Starkovskii, A. Yu., Ignition with Low-Temperature Plasma: Kinetic Mechanism and Experimental Verification, High Energy Chemistry 2009 43(3), 213
9. Ombrello, T., Won, S.H., Ju, Y., and Williams, S., Propagation Enhancement by Plasma Excitation of Oxygen Part I: Effects of O_3, Combustion and Flame 157 (2010) 1906-1915;
10. Ombrello, T., Won, S.H., Ju, Y., and Williams, S., 2009, Flame propagation enhancement by plasma excitation of oxygen. Part II: Effects of $O_2(a^1\Delta)$, Combustion and Flame 157 (2010) 1916–1928
11. Michael, J.B., Chng, T.L, Miles, R.B., Sustained Propagation of Ultra-Lean Methane/Air Flames with Pulsed Microwave Energy Deposition, Combustion and Flame 2013 160, 796-807.
12. Marcum, S.D., Ganguly, B.N., Electric-Field-Induced Flame Speed Enhancement, Combustion and Flame 2005 143, 27-36
13. Dutta A., Yin Z., and Adamovich I.V., Cavity Ignition and Flameholding of Ethylene-Air and Hydrogen-Air Flows by a Repetitively Pulsed Nanosecond Discharge, Combustion and Flame, vol. 158, 2011, pp. 1564-1576
14. Pilla, G., Galley, D., Lacoste, D.A., Lacas, F., Veynante, D., and Laux, C.O., Stabilization of a Turbulent Premixed Flame Using a Nanosecond Repetitively Pulsed Plasma IEEE Transactions on Plasma Science, 2006 34, 2471

15. Pilla, G., Lacoste, D.A., Veynante, D., and Laux, C.O., Stabilization of a Swirled Propane-Air Flame Using a Nanosecond Repetitively Pulsed Plasma IEEE Transactions on Plasma Science, 2008 36(4), 940
16. Hemawan, K.W., Wichman, I.S., Lee, T., Grotjohn, T.A., Asmussen, J., Compact Microwave Re-Entrant Cavity Applicator for Plasma-Assisted Combustion, Review of Scientitic Instruments, 2009 80, 053507
17. Smirnov, V.V., Stelmakh, O.M., Fabelinsky, V.I., Kozlov, D.N., Starik, A.M., and Titova, N.S., On the Influence of Electronically Excited Oxygen Molecules on Combustion of Hydrogen–Oxygen Mixture, Journal of Physics D: Applied Physics, 2008 41, 192001.
18. Mintusov, E., Serdyuchenko, A., Choi, I., Lempert, W.R., and Adamovich, I.V., Mechanism of Plasma Assisted Oxidation and Ignition of Ethylene-Air Flows by a Repetitively Pulsed Nanosecond Discharge, Proceedings of the Combustion Institute, 2009 32, 3181
19. Uddi, M., Jiang, N., Mintusov, E., Adamovich, I.V., and Lempert, W.R., Atomic Oxygen Measurements in Air and Air/Fuel Nanosecond Pulse Discharges by Two Photon Laser Induced Fluorescence, Proceedings of the Combustion Institute, 2009 32, 929
20. Lou, G., Bao, A., Nishihara. M., Keshav. S., Utkin. Y. G., Rich. J. W., Lempert, W. R., and Adamovich, I.V., Ignition of premixed hydrocarbon–air flows by repetitively pulsed, nanosecond pulse duration plasma, Proceedings of the Combustion Institute, Vol. 31, 2007, pp. 3327-3334
21. Yin Z., Montello A., Carter C.D., Lempert W.R., and Adamovich I.V., Measurements of Temperature and Hydroxyl Radical Generation / Decay in Lean Fuel-Air Mixtures Excited by a Repetitively Pulsed Nanosecond Discharge, Combustion and Flame, vol. 160, 2013, pp. 1594-1608
22. Yin Z., Adamovich I.V., and Lempert W.R., OH Radical and Temperature Measurements During Ignition of H2-Air Mixtures Excited by a Repetitively Pulsed Nanosecond Discharge, Proceedings of the Combustion Institute, vol. 34, 2013, pp. 3249–3258
23. Yin Z., Takashima K., and Adamovich I.V., Ignition Time Measurements in Repetitive Nanosecond Pulse Hydrogen-Air Plasmas at Elevated Initial Temperatures, IEEE Transactions on Plasma Science, vol. 39, 2011, pp. 3269-3282
24. Nagaraja S., Yang V., Yin Z., and Adamovich I., Ignition of Hydrogen-Air Mixtures using Pulsed Nanosecond Dielectric Barrier Plasma Discharges in Plane-to-Plane Geometry, Combustion and Flame, vol. 161, 2014, pp. 1026-1037
25. Kim, W., Do, H., Mungal, G., and Cappelli, M.A. A Study of Plasma Stabilized Diffusion Flames at Elevated Ambient Temperatures. IEEE Trans. Plasma Sci. 2008 36(6), 2989.
26. Kim, W., Mungal, G.M., and Cappelli, M.A., The role of in situ reforming in plasma enhanced ultra lean premixed methane/air flames. Combust. Flame, 2010 157(2) 374
27. Rao, X., Hammack, S., Lee, T., Carter, C., and Matveev, I.B. Combustion Dynamics of Plasma-Enhanced Premixed and Nonpremixed Flames. IEEE Trans. Plasma Sci. 2010 38(12), 3265
28. Rao, X., Hammack, S., Carter, C., Grotjohn, T., Asmussen, J., and Lee, T., Microwave-Plasma-Coupled Re-Ignition of Methane-and-Oxygen Mixture Under Auto-Ignition Temperature. IEEE Trans. Plasma Sci. 39(12), 3307

29. Sun, W., Uddi, M., Ombrello, T., Won, S.H., Carter, C.D., and Ju, Y. Effects of Non-Equilibrium Plasma Discharge of Counterflow Diffusion Flame Extinction. Proc. Combust. Inst. 33(2), 3211
30. Sun, W., Uddi, M., Won, S.H., Ombrello, T., C.D. Carter, Carter, C.D., and Ju, Y. Kinetic Effects of Non-Equilibrium Plasma-Assisted Methane Oxidation on Diffusion Flame Extinction Limits. Combust. Flame, 159, 221
31. Sun, W., Won, S., Ombrello, T., Carter, C., Ju, Y., Direct ignition and S-curve transition by in situ nano-second pulsed discharge in methane/oxygen/helium counterflow flame. Proceedings of the Combustion Institute. Volume 34, Issue 1, 2013, Pages 847–855
32. Nagaraja S., Li T., Sutton J., Adamovich I., and Yang V., Nanosecond Plasma Enhanced H2/O2/N2 Premixed Flat Flames, Proceedings of the Combustion Institute, vol. 35, 2015, pg. 3471–3478
33. Li T., Adamovich I.V., and Sutton J.A., A Burner Platform for Examining the Effects of Non-Equilibrium Plasmas on Oxidation and Combustion Chemistry, Combustion Science and Technology, vol. 185, 2013, pp. 990-998
34. HOLTHUIS & ASSOCIATES, www.flatflame.com, website accessed July, 2015
35. Adamovich, I.V., Lempert, W.R., Nishihara, M., Rich, J.W., Utkin, Y.G., Repetitively Pulsed Nonequilibrium Plasmas for Magnetohydrodynamic Flow Control and Plasma-Assisted Combustion, Journal of Propulsion and Power, 2008 24(6), 1198
36. Kee R. J., Grcar J. F., Smooke M. D., Miller J. A., PREMIX: a fortran program for modeling steady laminar one-dimensional premixed flames, Sandia National Laboratories report, 1985.
37. Kee R. J., Rupley F. M., Miller J. A., Coltrin M. E., Grcar J. F., Meeks E., Moffat H. K., Lutz A. E., Dixon-Lewis G., Smooke M. D., Warnatz J., Evans G. H., Larson R. S., Mitchell R. E., Petzold L. R., Reynolds W. C., Caracotsios M., Stewart W. E., Glarborg P., Wang C., and Adigun O., CHEMKIN Collection, Release 3.6, Reaction Design, Inc., San Diego, CA (2000)
38. Smith G. P., Golden D. M., Frenklach M., Moriarty N. W., Eiteneer B., Goldenberg M., Bowman C., Hanson R. K., Song S., Gardiner W. C., Jr., Lissianski V. V., and Qin Z. http://www.me.berkeley.edu/gri_mech/
39. German K.R., "Radiative and predissociative lifetimes of the V' =0, 1, and 2 levels of the A2Σ+ state of OH and OD", J. Chem. Phys. 63 (1975) 5252
40. Berg P.A., Hill D.A., Noble A.R., Smith G.P., Jeffries J.B., Crosley D.R., Combust. Flame 121 (2000) 223
41. Sutton, J.A., Williams, B.A., Fleming, J.W., Investigation of NCN and prompt-NO formation in low-pressure C1–C4 alkane flames, Combustion and Flame 159 (2012) 562–576
42. Sutton, J. A., Williams, B. A., Fleming, J. W., Laser-Induced Fluorescence Measurements of NCN in Low Pressure CH4/O2/N2 Flames and Its Role in Prompt NO Formation, Combustion and Flame 2008, 153(3), 465-478
43. Luque J. and Crosley D.R., LIFBASE: Database and Spectral Simulation Program (Version 2.1.1), SRI International Report MP 99-009 (1999)
44. Li, T., Adamovich, I.V., Sutton, J.A., Effects of Non-Equilibrium Plasmas on Low-Pressure, Premixed Flames. Part 2: O-atom, to be submitted to Combustion and Flame.

Figure Captions

1 – (Top) Photograph of low-pressure plasma-flame facility. (Bottom) Photograph of low-pressure $CH_4/O_2/N_2$ flame during plasma discharge operation. HVE = high-voltage electrode.

2 – Comparison of spatially-resolved OH mole fraction measurements with and without the presence of the upper electrode 40 mm above the burner surface for the ϕ = 1.07 $CH_4/O_2/N_2$ operating condition. It is noted that the presence of the upper electrode has no discernible effect on the OH profiles.

3 – (a) Single pulse voltage and current profiles of the plasma discharge generated by FID pulser. (b) Single pulse voltage and current profiles of the plasma discharge generated by Behlke pulser.

4 – (a) ICCD images of a single pulse discharge generated by FID pulser. FID operation was at 40 kHz repetition rate and the ICCD gate time was 10 ns. (b) ICCD images of single pulse discharge generated by Behlke pulser. Behlke operation was at 70 kHz repetition rate and the ICCD gate time was 200 ns. ICCD images were acquired for the ϕ = 1.07, $CH_4/O_2/N_2$ case.

5 – Schematic of OH LIF diagnostic system for measurements within the low-pressure plasma/flame facility.

6 – (Top) ICCD image of 1D OH fluorescence signal and flame emission from the Φ = 1.07 $CH_4/O_2/N_2$ flame (b) OH fluorescence signal profile at 12 mm above the burner surface (black line). Red line corresponds to effective pathlength of uniform OH LIF signal as determined from the total integrated signal of the OH fluorescence signal (black line)

7 – OH excitation spectra at three different temperatures acquired from LIFBASE [44] (P=25 Torr, laser linewidth=0.046nm, Doppler broadening). Black line - without introducing noise, Red line - with noise at the same level as measured in OH LIF experiment.

8 – Boltzmann plot and inferred temperatures for the synthetic T = 1820 K case using full laser scale and integrated contributions of five rotational lines (black lines); fixed laser excitation at peak of rotational lines for a spectral resolution of 0.001 cm^{-1} (red lines); and fixed laser excitation at peak of rotational lines for a spectral resolution of 0.046 cm^{-1} (blue lines).

9 – Boltzmann plots obtained from the synthetic OH LIF spectra shown in Fig. 7 using five OH excitation rotational lines labeled in Fig. 7 with and without estimated experimental noise incorporated, for three different temperature values. “Best fit” inferred temperature value is shown for each case.

10 – Comparison of uncertainty in temperature inferred using 5-line and 4-line OH LIF thermometry with and without estimated experimental noise. Results are from simulated OH LIF spectra using LIFBASE [44].

11 – ICCD images of CH* emission from $CH_4/O_2/N_2$ flames for different equivalence ratios with and without electric discharge generated by the FID pulser.

12 – Intensity distributions of CH* emission along the centerline of the ICCD images, taken in $CH_4/O_2/N_2$ flames for different equivalence ratios, with and without electric discharge generated by the FID pulser, at same conditions as in Fig. 11.

13 – ICCD images of CH* emission in $C_2H_4/O_2/N_2$ flames for different equivalence ratios, with and without electric discharge generated by the FID pulser.

14 – Intensity distributions of CH* emission along the centerline of the ICCD images, taken in $C_2H_4/O_2/N_2$ flames for different equivalence ratios, with and without electric discharge generated by the FID pulser, at same conditions as in Fig. 13.

15 – Temperature and OH mole fraction profiles in methane flames for different equivalence ratios, at the same conditions as shown in Fig. 11, with and without discharge sustained by the FID and Belhke pulse generators. Solid lines are the least square fits to the temperature measurements and dashed lines correspond to Chemkin simulations of the OH mole fraction profiles without the plasma.

16 – Temperature difference and relative OH mole fraction difference $[(X_{OH\ Plasma}-X_{OH})/X_{OH}]$ in $CH_4/O_2/N_2$ flames for different equivalence ratios at the same conditions as in Figs. 11 and 15 with and without the discharge sustained by the FID and Belhke pulse generators.

17 – Temperature and OH mole fraction profiles in ethylene flames for different equivalence ratios, at the same conditions as shown in Fig. 13, with and without discharge sustained by the FID and Belhke pulse generators. Solid lines are the least square fits to the temperature measurements and dashed lines correspond to Chemkin simulations of the OH mole fraction profiles without the plasma.

18 – Temperature difference and relative OH mole fraction difference $[(X_{OH\ Plasma}-X_{OH})/X_{OH}]$ in $C_2H_4/O_2/N_2$ flames for different equivalence ratios at the same conditions as in Figs. 13 and 17 with and without the discharge sustained by the FID and Belhke pulse generators.

19 – Temperature and OH mole fraction profiles in hydrogen flames for different equivalence ratios at P = 25 Torr, with and without discharge sustained by the FID and Belhke pulse generators. Solid lines are the least square fits to the temperature measurements and dashed lines correspond to Chemkin simulations of the OH mole fraction profiles without the plasma.

20 – Temperature difference and relative OH mole fraction difference $[(X_{OH\ Plasma}-X_{OH})/X_{OH}]$ in $H_2/O_2/N_2$ flames for different equivalence ratios at the same conditions as in Fig. 19 with and without the discharge sustained by the FID and Belhke pulse generators.

Table 1 – Operating Conditions for Low-Pressure Flames

Flame	Equivalence Ratio		O_2/O_2+N_2	Fuel (slpm)	O_2 (slpm)	N_2 (slpm)	Pressure (Torr)
CH_4 Flames	Standard	1.07	0.3	0.45	0.84	1.93	25
	Lean	0.81	0.3	0.34	0.84	1.93	25
	Ultra-lean	0.62	0.3	0.26	0.84	1.93	25
C_2H_4 Flames	Standard	1.07	0.3	0.3	0.84	1.93	25
	Lean	0.81	0.3	0.227	0.84	1.93	25
	Ultra-lean	0.52	0.3	0.146	0.84	1.93	25
H_2 Flames	Lean	0.81	0.3	0.68	0.42	0.965	25
	Ultra-lean	0.5	0.3	0.42	0.42	0.965	25

Table 2– Parameters for Temperature Profiles, Eq. (2)

	Φ	Pulser	A	B	C	D	E
CH_4 /O_2/N_2	1.07	No Plasma	540.53	1305.1	-0.14339	1.5842	-0.17125
	1.07	Belhke	539.68	1356	-0.18768	1.3792	-0.12407
	1.07	FID	541.1	1458	-0.17888	1.4725	-0.13783
	0.81	No Plasma	465.45	1383	-0.06835	1.9043	-0.17563
	0.81	Belhke	455.49	1347.7	-0.21735	1.3286	-0.02427
	0.81	FID	454.02	1387.6	-0.21939	1.2847	0.056516
	0.62	No Plasma	408.29	1203.9	-0.02389	2.152	-0.14519
	0.62	Belhke	403.81	1300.9	-0.11193	1.5676	0.061834
	0.62	FID	405.21	1237.8	-0.13882	1.5187	0.10561
C_2H_4/O_2/N_2	1.07	No Plasma	618.89	1195.2	-0.3088	1.3036	-0.17414
	1.07	Belhke	622.78	1152.2	-0.44925	1.1665	-0.10949
	1.07	FID	625.61	1251.6	-0.29556	1.2927	0.027859
	0.81	No Plasma	500.28	1054.8	-0.42074	1.1664	0.062835
	0.81	Belhke	501.95	1180.6	-0.50782	1.0352	-0.00402
	0.81	FID	503.1	1211.1	-0.34297	1.2289	0.059336
	0.52	No Plasma	403.33	1028.4	-0.18965	1.4246	0.074025
	0.52	Belhke	403.79	1020.1	-0.33601	1.1414	0.12811
	0.52	FID	403.54	1118.3	-0.30796	1.266	0.08229
H_2/O_2/N_2	0.81	No Plasma	498.54	7059.4	-0.01349	1.069	-2.4172
	0.81	Belhke	500.4	7418.7	-0.01652	0.9928	-2.1385
	0.81	FID	502.52	1426.9	-0.05879	1.3055	-0.4509
	0.50	No Plasma	405.07	2887.8	-0.0278	1.1003	-1.3912
	0.50	Belhke	406.61	5038.6	-0.02906	0.8967	-1.4621
	0.50	FID	406.17	1630.8	-0.05173	1.2498	-0.62405

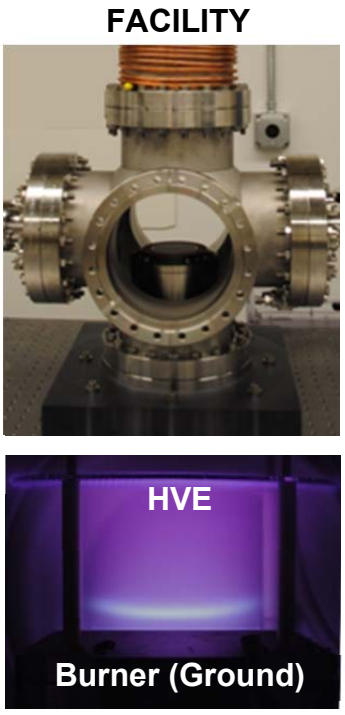

Figure 1

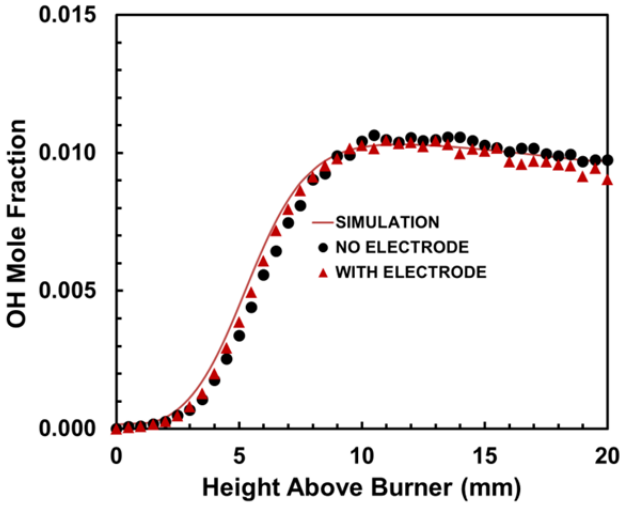
0.015
0.010
0.005
0.000
OH Mole Fraction
0
5
10
15
20
Height Above Burner (mm)
SIMULATION
NO ELECTRODE
WITH ELECTRODE

Figure 2

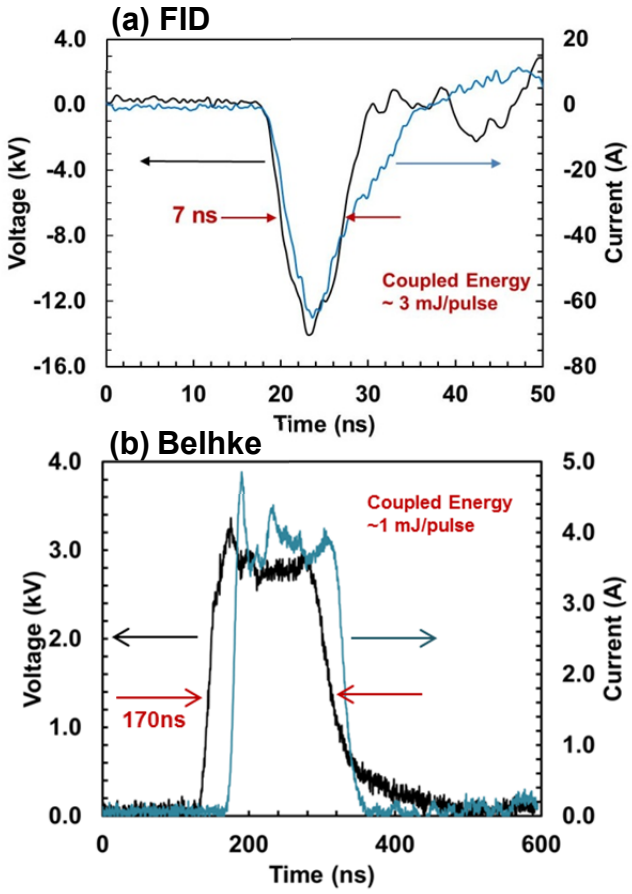
(a) FID
Voltage (kV)
Current (A)
Time (ns)
7 ns
Coupled Energy
~ 3 mJ/pulse
(b) Belhke
Voltage (kV)
Current (A)
Time (ns)
170ns
Coupled Energy
~1 mJ/pulse

Figure 3

(a) FID

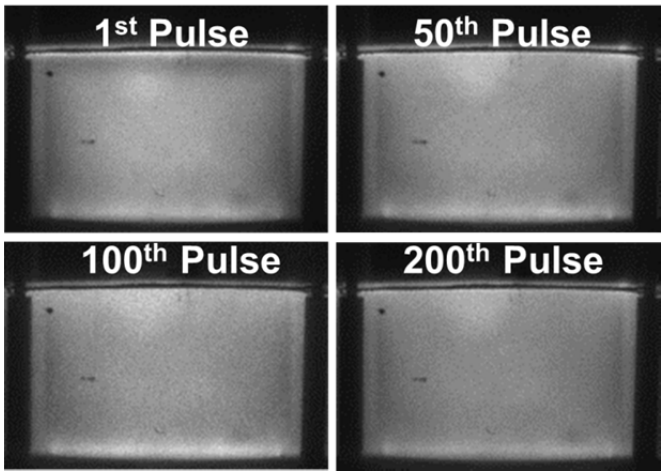

(b) Belhke

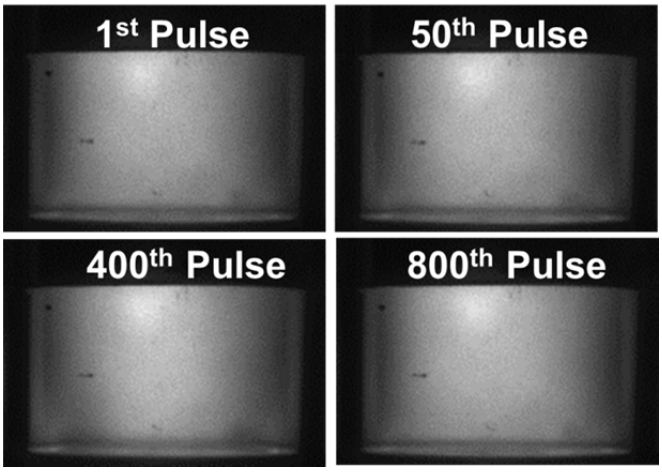

Figure 4

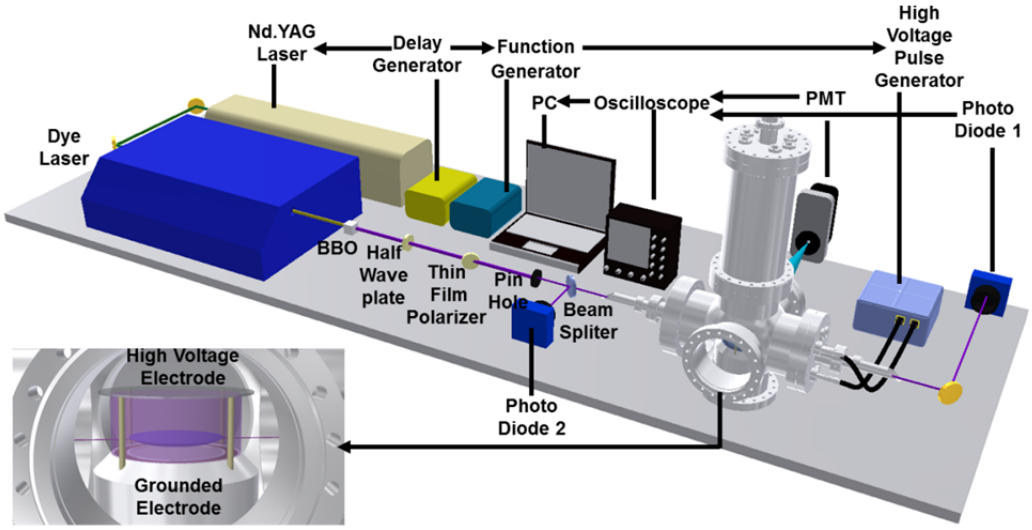
Nd.YAG Laser
Delay Generator
Function Generator
High Voltage Pulse Generator
PC
Oscilloscope
PMT
Photo Diode 1
Dye Laser
BBO
Half Wave plate
Thin Film Polarizer
Pin Hole
Beam Spliter
Photo Diode 2
High Voltage Electrode
Grounded Electrode

Figure 5

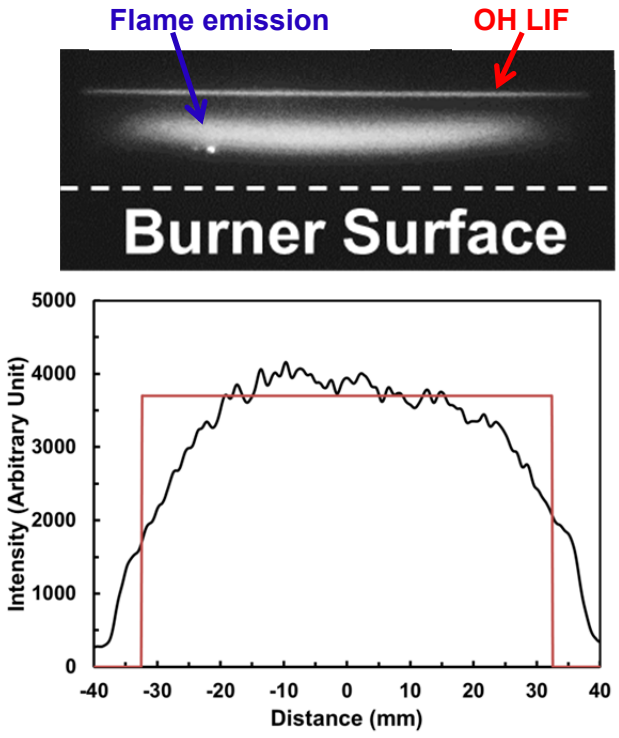
Flame emission
OH LIF
Burner Surface
Intensity (Arbitrary Unit)
5000
4000
3000
2000
1000
0
-40
-30
-20
-10
0
10
20
30
40
Distance (mm)

Figure 6

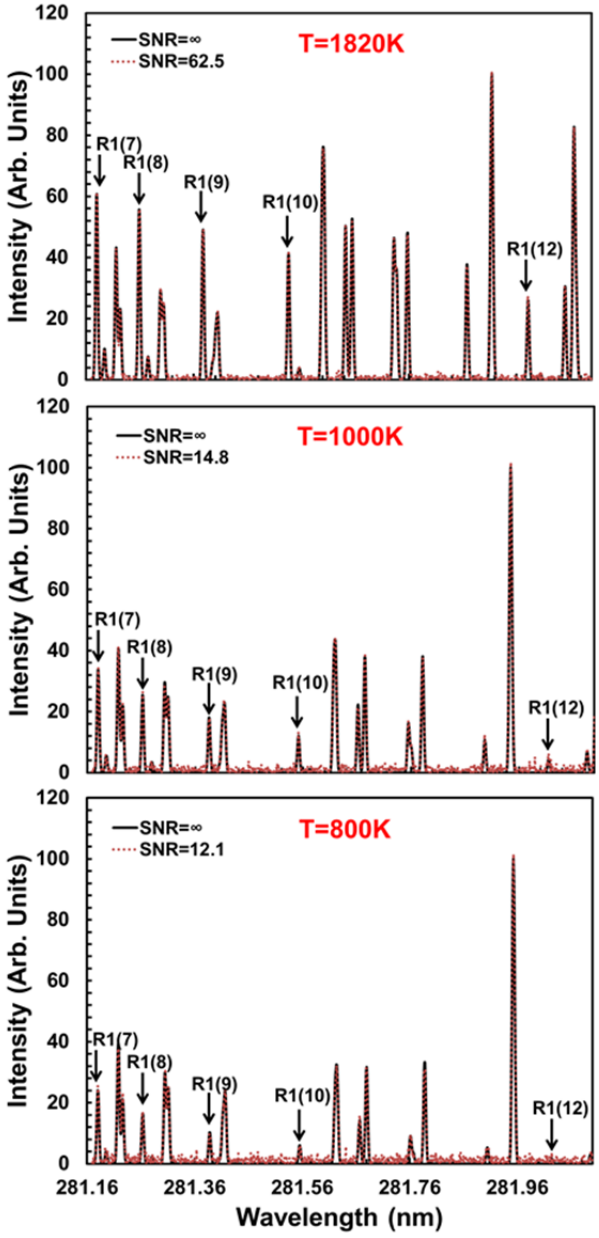
T=1820K
SNR=∞
SNR=62.5
T=1000K
SNR=∞
SNR=14.8
T=800K
SNR=∞
SNR=12.1
R1(7)
R1(8)
R1(9)
R1(10)
R1(12)
Intensity (Arb. Units)
Wavelength (nm)
0
20
40
60
80
100
120
281.16
281.36
281.56
281.76
281.96

Figure 7

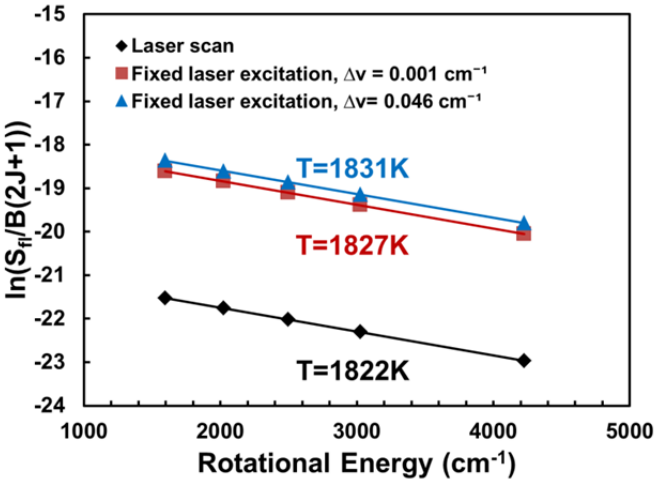
Laser scan
Fixed laser excitation, Δv = 0.001 cm⁻¹
Fixed laser excitation, Δv= 0.046 cm⁻¹
T=1831K
T=1827K
T=1822K
ln(S_fl/B(2J+1))
Rotational Energy (cm-1)
-15
-16
-17
-18
-19
-20
-21
-22
-23
-24
1000
2000
3000
4000
5000

Figure 8

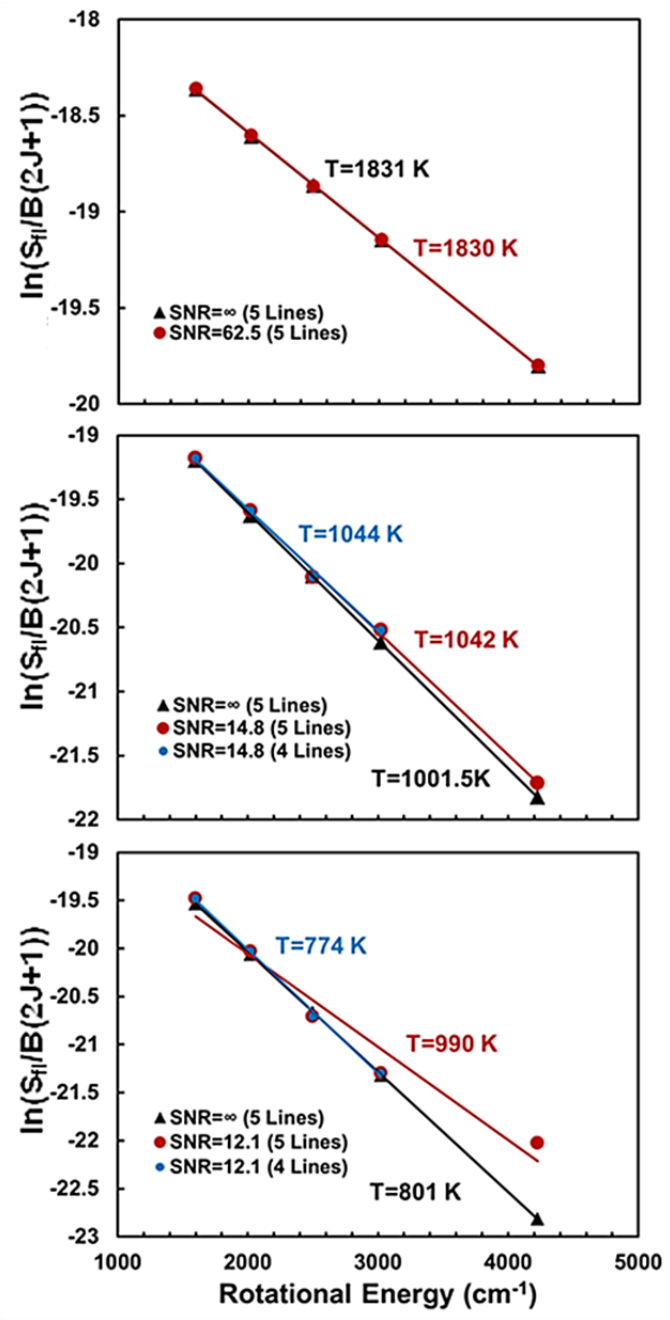
-18
-18.5
-19
-19.5
-20
ln(Sfi/B(2J+1))
T=1831 K
T=1830 K
▲SNR=∞ (5 Lines)
●SNR=62.5 (5 Lines)
-19
-19.5
-20
-20.5
-21
-21.5
-22
ln(Sfi/B(2J+1))
T=1044 K
T=1042 K
▲SNR=∞ (5 Lines)
●SNR=14.8 (5 Lines)
●SNR=14.8 (4 Lines)
T=1001.5K
-19
-19.5
-20
-20.5
-21
-21.5
-22
-22.5
-23
ln(Sfi/B(2J+1))
T=774 K
T=990 K
▲SNR=∞ (5 Lines)
●SNR=12.1 (5 Lines)
●SNR=12.1 (4 Lines)
T=801 K
1000
2000
3000
4000
5000
Rotational Energy (cm-1)

Figure 9

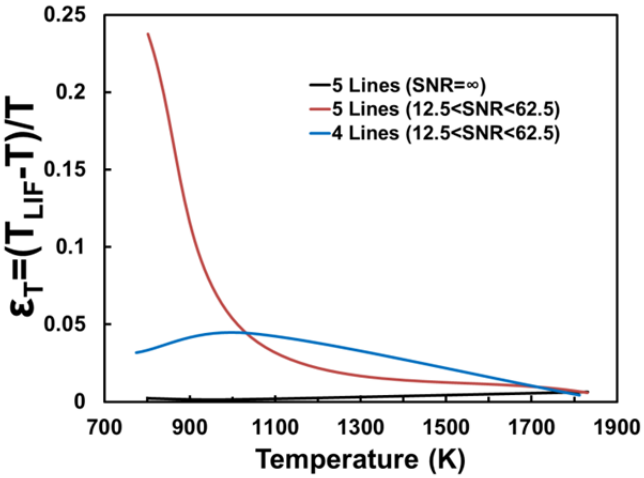
0.25
0.2
0.15
0.1
0.05
0
700
900
1100
1300
1500
1700
1900
Temperature (K)
$\varepsilon_T=(T_{LIF}-T)/T$
5 Lines (SNR=∞)
5 Lines (12.5<SNR<62.5)
4 Lines (12.5<SNR<62.5)

Figure 10

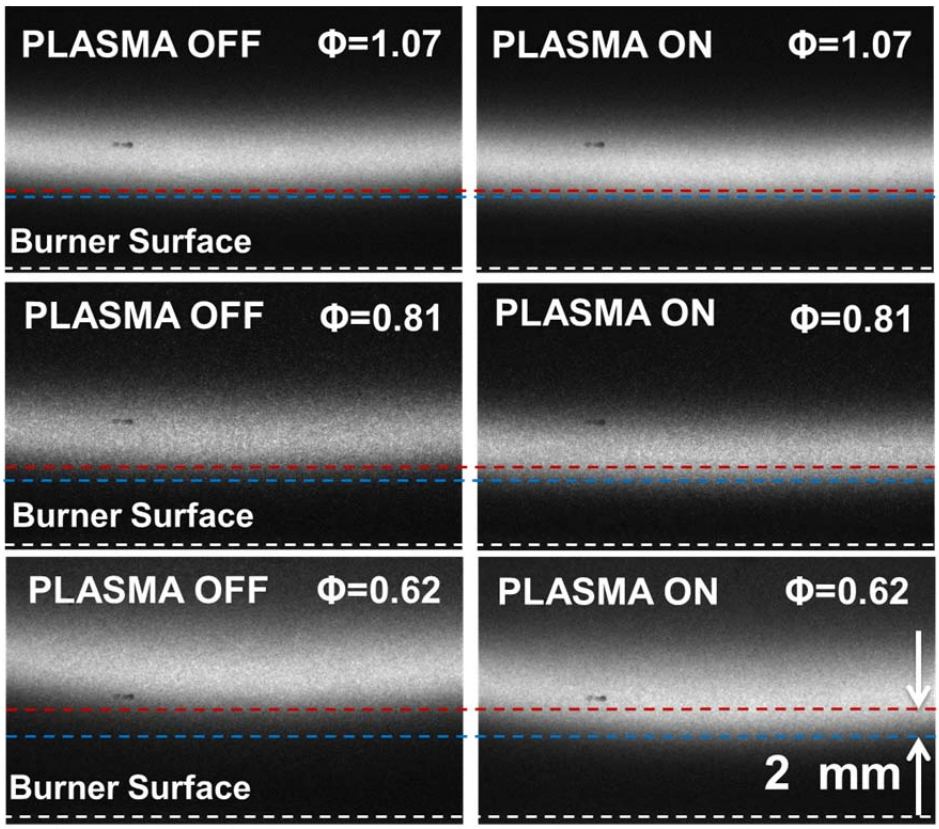
PLASMA OFF Φ=1.07
PLASMA ON Φ=1.07
Burner Surface
PLASMA OFF Φ=0.81
PLASMA ON Φ=0.81
Burner Surface
PLASMA OFF Φ=0.62
PLASMA ON Φ=0.62
Burner Surface
2 mm

Figure 11

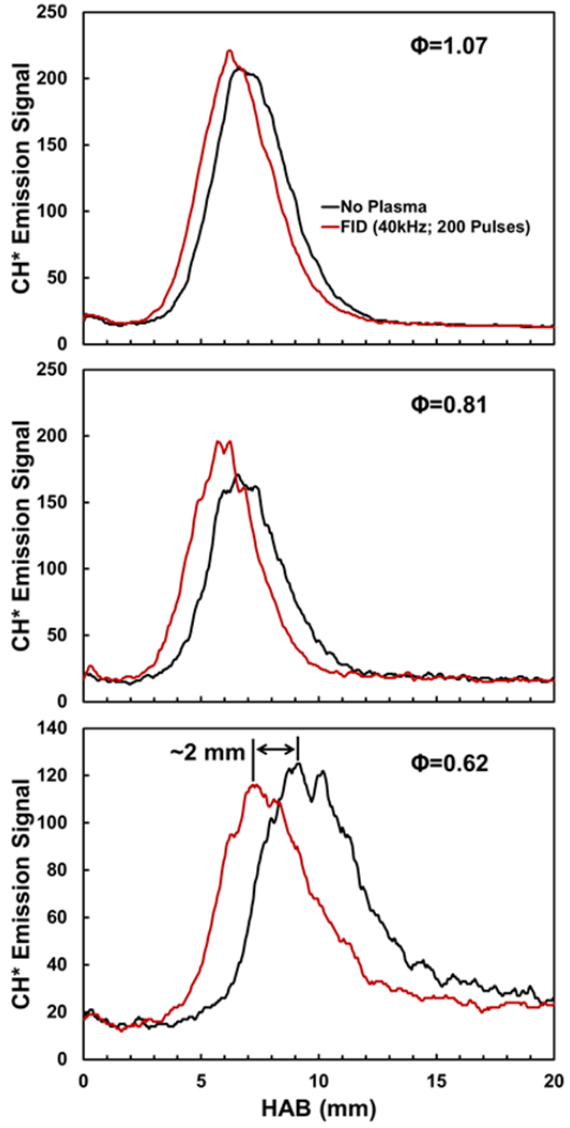
Φ=1.07
No Plasma
FID (40kHz; 200 Pulses)
Φ=0.81
~2 mm
Φ=0.62
CH* Emission Signal
HAB (mm)

Figure 12

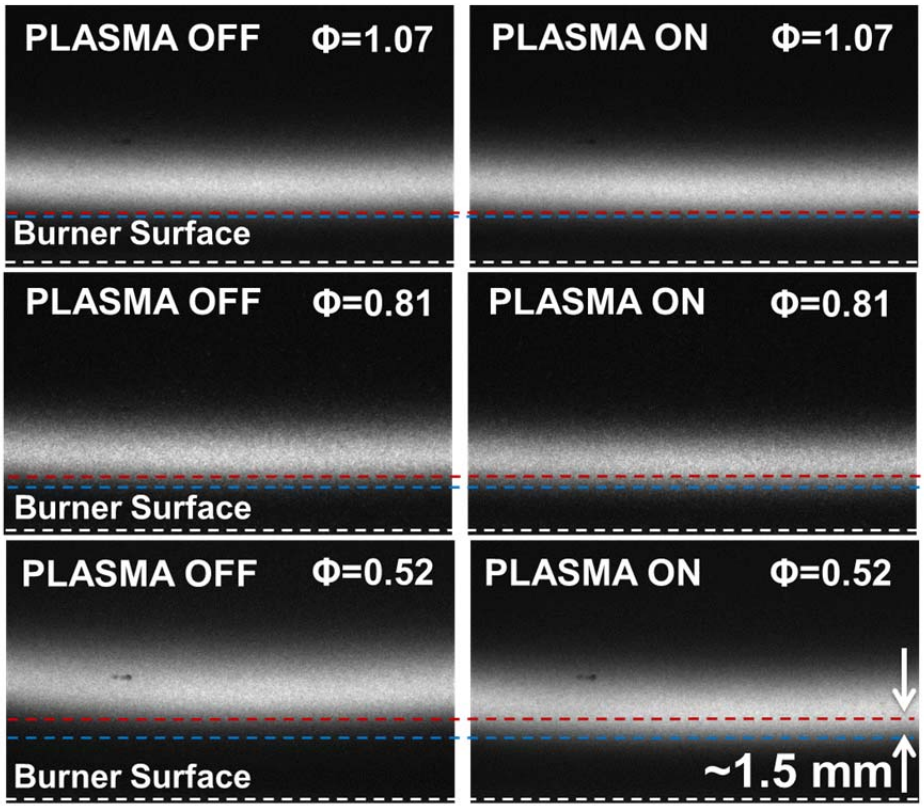
PLASMA OFF Φ=1.07
PLASMA ON Φ=1.07
Burner Surface
PLASMA OFF Φ=0.81
PLASMA ON Φ=0.81
Burner Surface
PLASMA OFF Φ=0.52
PLASMA ON Φ=0.52
Burner Surface
~1.5 mm

Figure 13

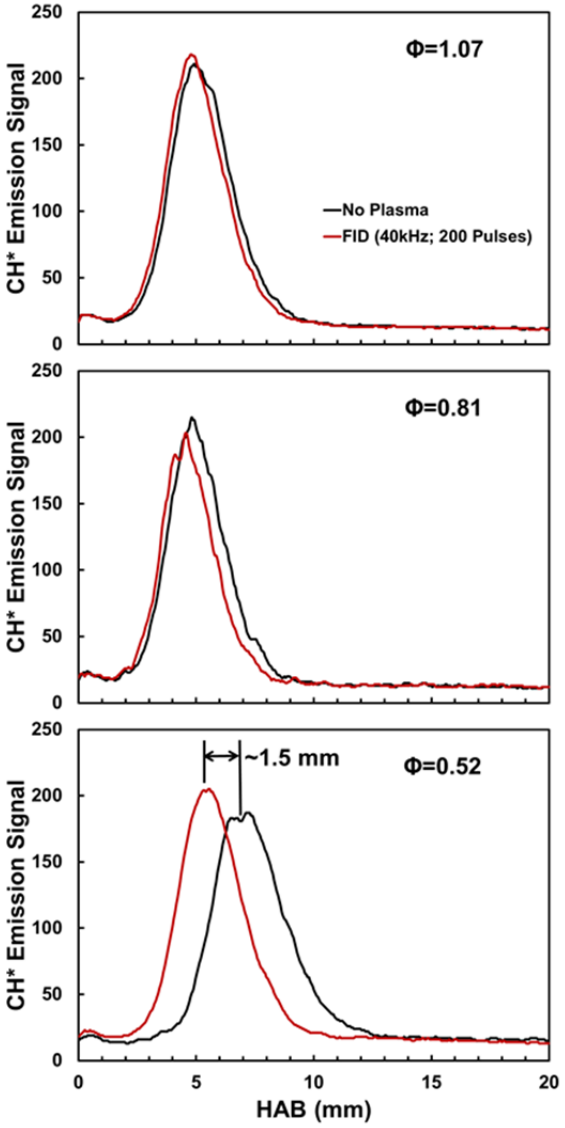
Φ=1.07
No Plasma
FID (40kHz; 200 Pulses)
Φ=0.81
~1.5 mm
Φ=0.52
CH* Emission Signal
HAB (mm)
0
50
100
150
200
250
5
10
15
20

Figure 14

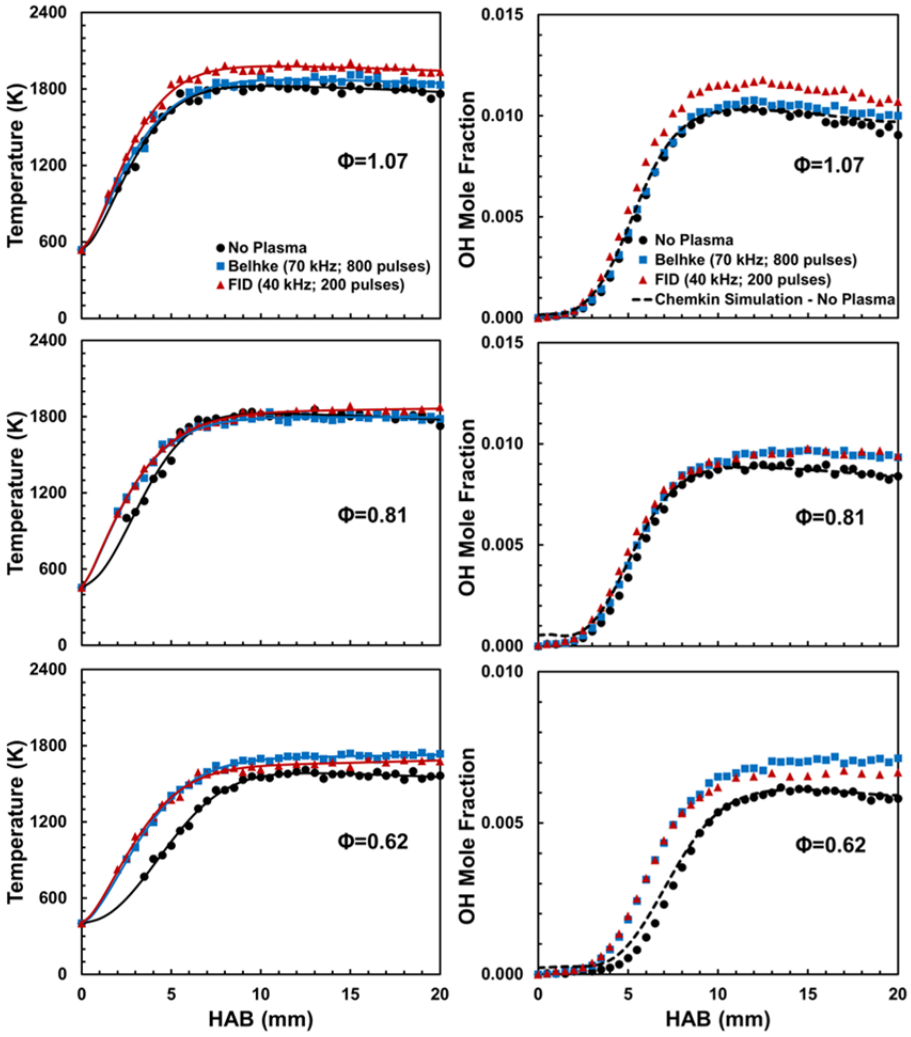
Temperature (K)
OH Mole Fraction
HAB (mm)
Φ=1.07
Φ=0.81
Φ=0.62
No Plasma
Belhke (70 kHz; 800 pulses)
FID (40 kHz; 200 pulses)
Chemkin Simulation - No Plasma

Figure 15

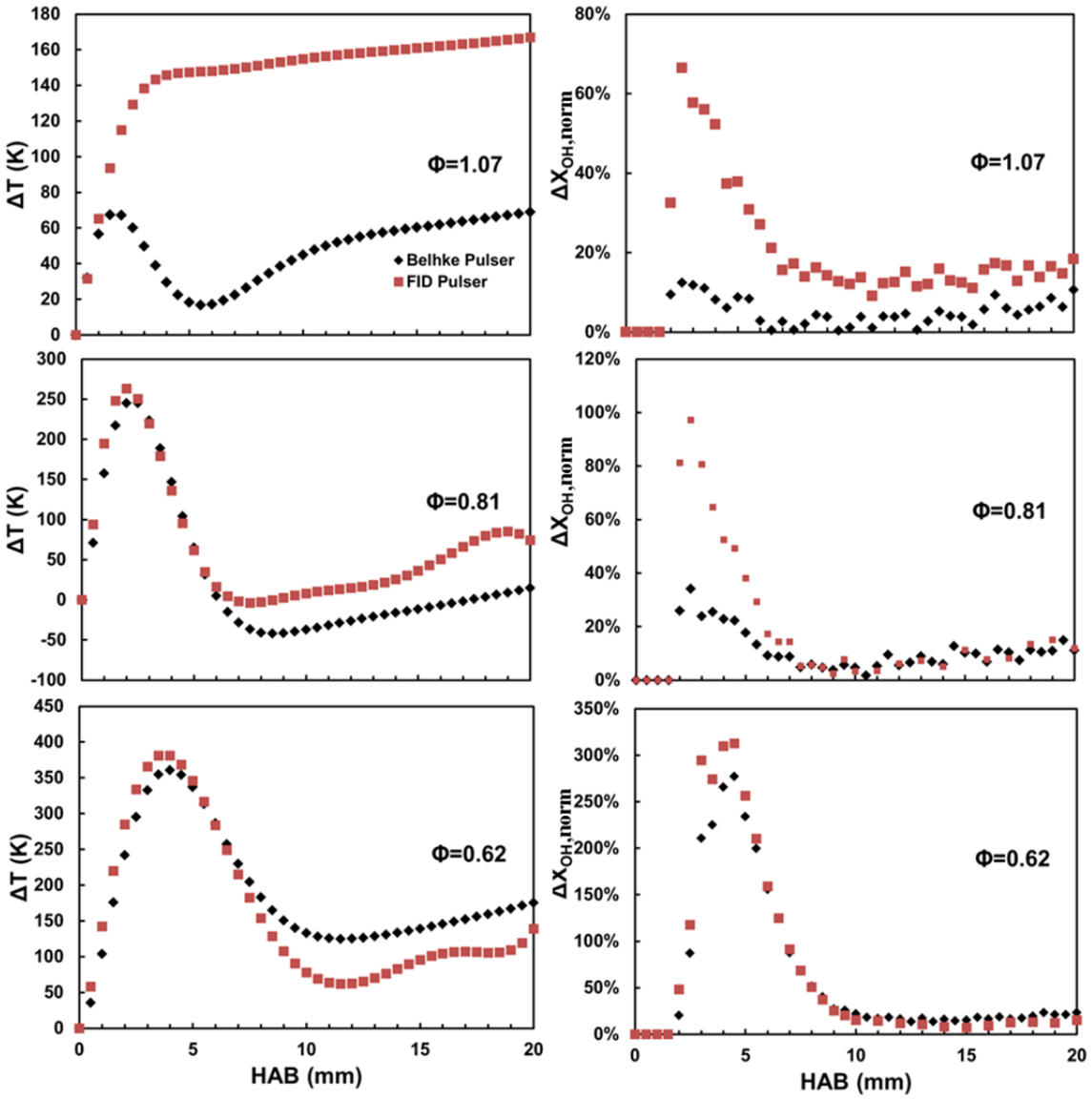
ΔT (K)
Φ=1.07
Belhke Pulser
FID Pulser
ΔX_OH,norm
Φ=1.07
Φ=0.81
Φ=0.81
Φ=0.62
Φ=0.62
HAB (mm)
HAB (mm)

Figure 16

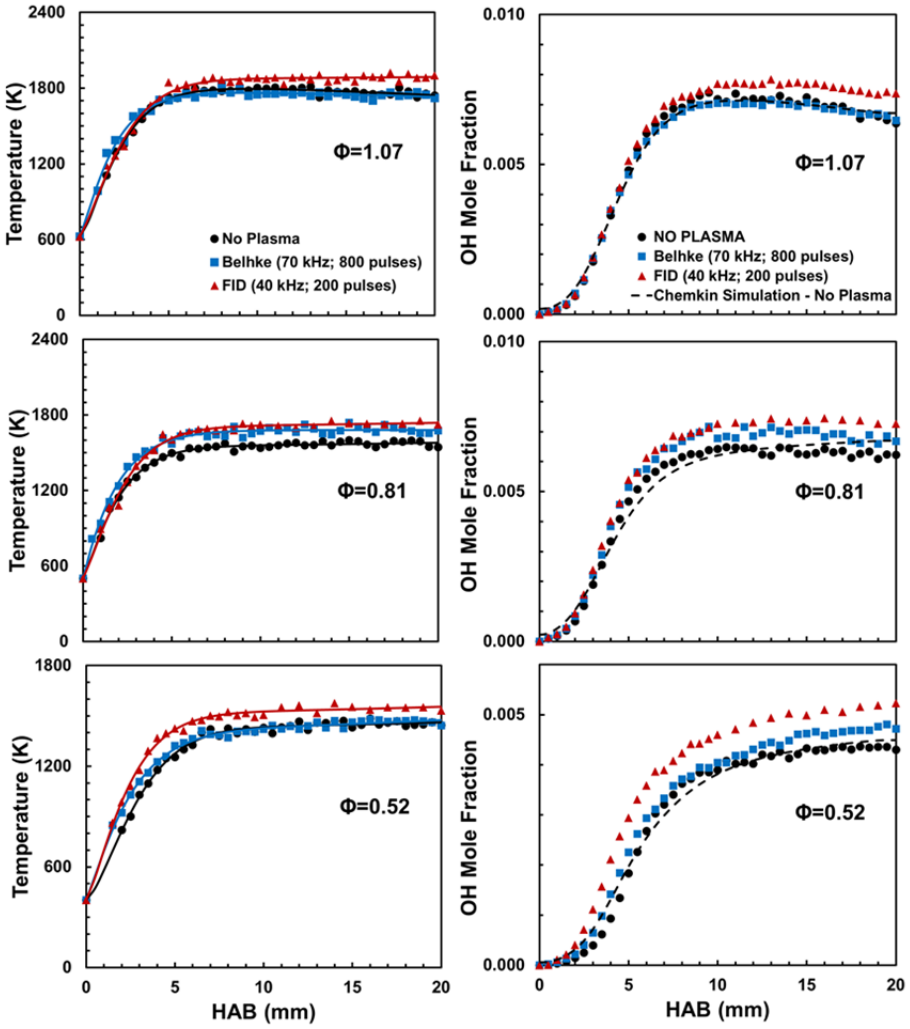
Temperature (K)
OH Mole Fraction
Φ=1.07
Φ=0.81
Φ=0.52
No Plasma
Belhke (70 kHz; 800 pulses)
FID (40 kHz; 200 pulses)
NO PLASMA
Chemkin Simulation - No Plasma
HAB (mm)

Figure 17

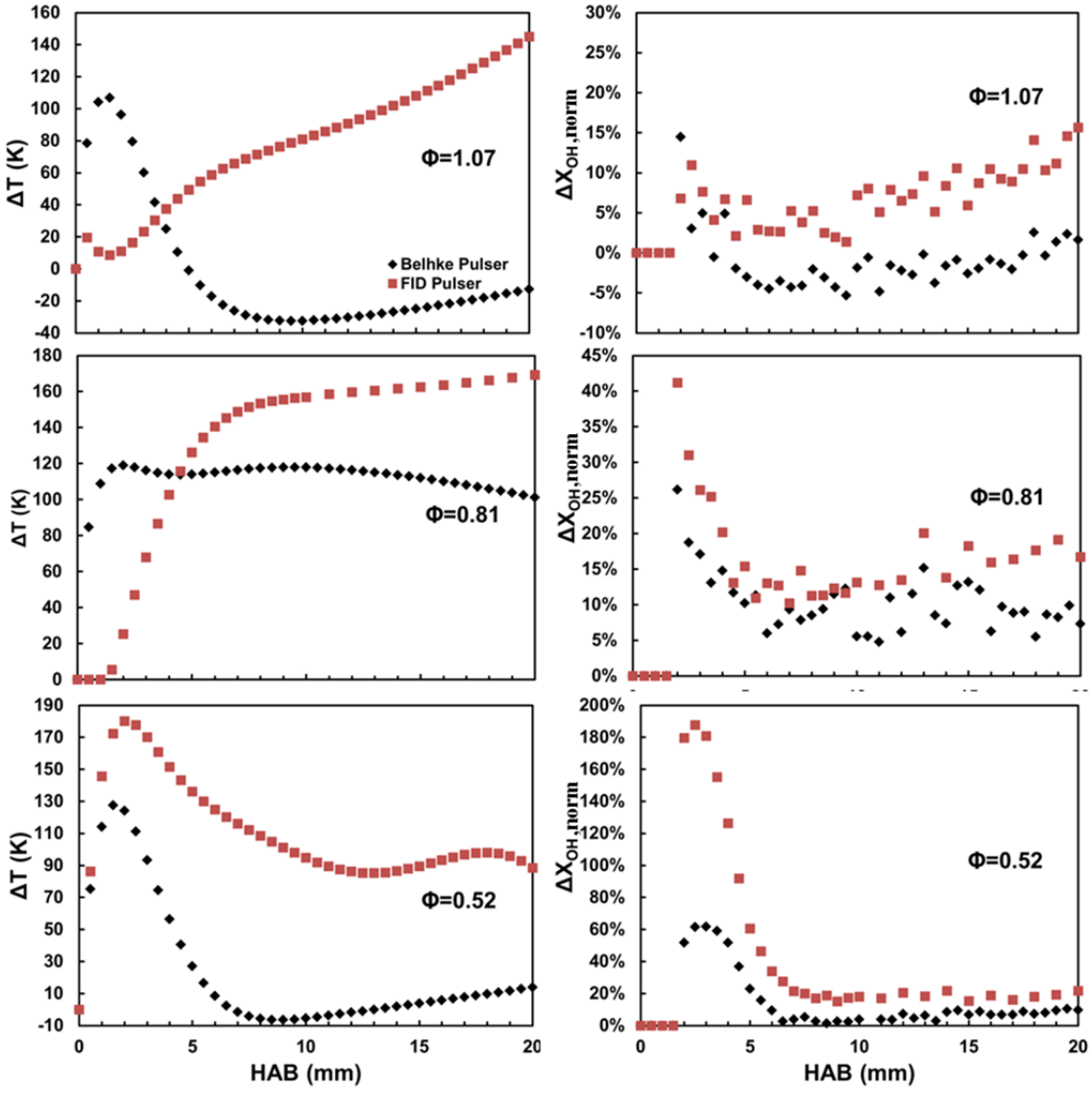
ΔT (K)
Φ=1.07
Belhke Pulser
FID Pulser
$\Delta X_{OH,norm}$
Φ=1.07
Φ=0.81
Φ=0.52
HAB (mm)
HAB (mm)

Figure 18

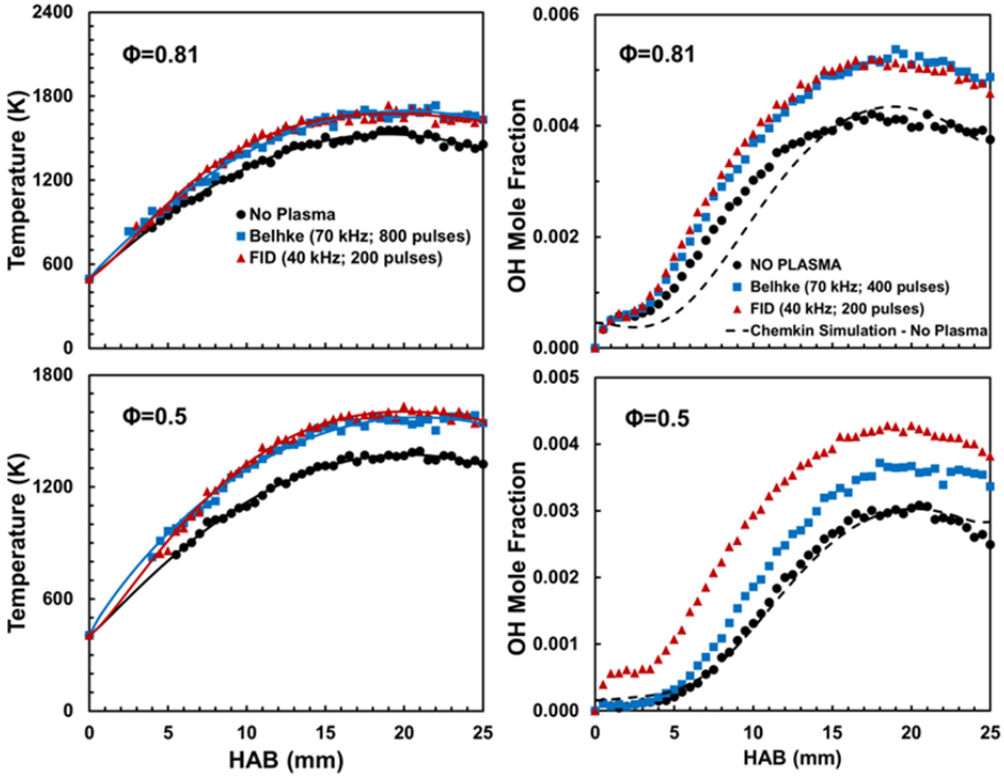
Φ=0.81
Temperature (K)
No Plasma
Belhke (70 kHz; 800 pulses)
FID (40 kHz; 200 pulses)
OH Mole Fraction
NO PLASMA
Chemkin Simulation - No Plasma
Φ=0.5
HAB (mm)

Figure 19

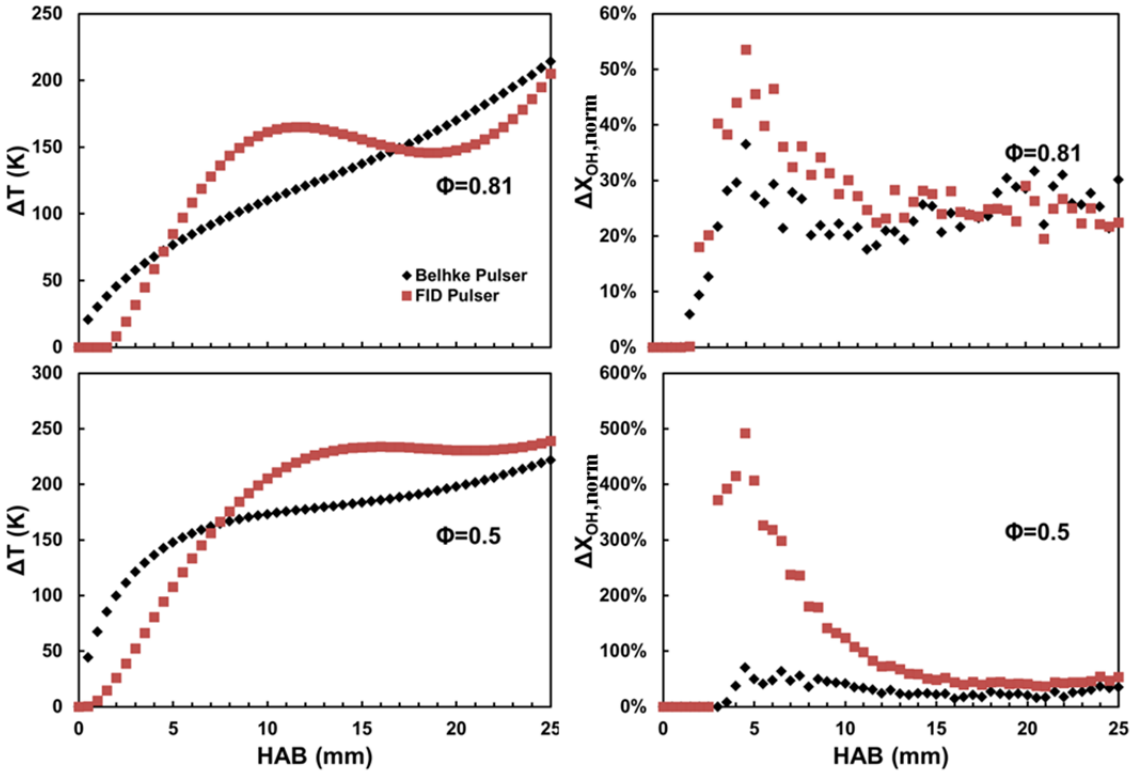
ΔT (K)
Φ=0.81
Belhke Pulser
FID Pulser
ΔX_OH,norm
Φ=0.81
ΔT (K)
Φ=0.5
ΔX_OH,norm
Φ=0.5
HAB (mm)
HAB (mm)

Figure 20